Estudio experimental y numérico de propiedades termomecánicas y durabilidad del asfalto en frío

Proyecto final para optar al grado de Ingeniería Mecánica

Autor: Imanol Barreiro (barreiroima@gmail.com)

Director: Dr. Ing. Amadeo Daniel Sosa

Mar del Plata, noviembre 2024

Estudio experimental y numérico de propiedades termomecánicas y durabilidad del asfalto en frío

Proyecto final para optar al grado de Ingeniería Mecánica

Autor: Imanol Barreiro (barreiroima@gmail.com)

Director: Dr. Ing. Amadeo Daniel Sosa

Mar del Plata, noviembre 2024

Contents

List of Figures

List of Tables

Standard references

NF EN 13043, *Aggregates for bituminous mixtures and surface treatments for roads, airfields and other trafficked areas.*

NF EN 12591, *Specifications for paving grade bitumens.*

NF EN 12597, *Bitumen and Bituminous Binders — Terminology.*

NF EN 13924, *Bitumen and bituminous binders—Specification framework for special paving grade bitumen — Part 2: Multigrade paving grade bitumens.*

NF EN 1428, *Bitumen and bituminous binders - Determination of water content bitumen emulsions - Azeotropic distillation method.*

NF EN 13808, *Bitumen and bituminous binders - Framework for specifying cationic bituminous emulsions.*

NF EN 933-1, *Tests for geometrical properties of aggregates-Part 1: Determination of particle size distribution — Sieving method.*

NF EN 12846-1, *Bitumen and bituminous binders - Determination of efflux time by the efflux viscometer- Part 1: bituminous emulsions.*

NF EN 1426, *Bitumen and bituminous binders - Determination of needle penetration.*

NF EN 1427, *Bitumen and bituminous binders - Determination of the softening point - Ring and Ball method.*

NF EN 12593, *Bitumen and bituminous binders — Determination of the Fraass breaking point.*

NF EN 12697-1, *Bituminous mixtures - Test methods - Part 1: soluble binder content.*

NF EN 12697-2, *Bituminous mixtures - Test methods - Part 2: determination of particle size distribution.*

NF EN 12697-5, *Bituminous mixtures - Test methods - Part5 : determination of the maximum density.*

NF EN 12697-31, *Bituminous mixtures - Test methods - Part 31: specimen preparation by gyratory compactor.*

NF EN 12697-54 Bituminous mixtures - Test methods - Part 54 : curing of specimen for test of mixtures with bitumen emulsion

NF EN 12697-22, *Bituminous mixtures - Test methods - Part 12: Rutting test.*

NF EN 12697-26, *Bituminous mixtures - Test methods - Part 26: Stiffness.*

NF EN 12697-44, *Bituminous mixtures - Test methods - Part 44: crack propagation by semi-circular bending test.*

NF EN 13108-1, *Bituminous mixtures - Material specifications - Part 1: asphalt concrete.*

NF EN 12697-35, *Bituminous mixtures — Test methods — Part 35: Laboratory mixing.*

NF P 98-150-2, *Cold Mix Asphalt - Construction of Pavement Foundations, Binder Courses, and Wearing Courses - Part 2: Cold Mix Asphalt — Constituents, Formulation, Manufacturing, Transport, Implementation, and On-Site Control.*

Resumen

Al hablar de construcción y mantenimiento de carreteras, el asfalto surge como un material frecuentemente empleado. Históricamente, el asfalto en caliente ha sido la opción preferida. Sin embargo, en los últimos años, el asfalto en frío ha ganado atención debido a sus características y ventajas únicas.
Una de las razones es la descarbonización de la industria de la construcción, que es uno de los objetivos para las próximas décadas. El uso de asfalto en frío es uno de los medios para alcanzar este objetivo debido a su muy bajo impacto en el medio ambiente. Sin embargo, su comportamiento mecánico en una etapa temprana, su envejecimiento y su reciclaje no son muy conocidos.
El asfalto en frío se crea utilizando emulsión de betún, una mezcla de betún (35-75 %), agua (25-65 %) y aditivos (1 %), combinada con agregados. Gracias a la emulsión de betún, la mezcla se puede aplicar y compactar a bajas temperaturas, ofreciendo una ventaja sobre el asfalto convencional, que debe mantenerse a 130-180°C durante la colocación y a 150-180°C durante el transporte. Este requisito de alta temperatura resulta en un consumo significativo de energía y por lo tanto en una gran emisión de carbono.
A pesar de sus ventajas, tales como, rápida aplicación, bajo costo de fabricación, transporte y aplicación, entre otras, las propiedades y el comportamiento viscoelástico del asfalto en frío lo hacen menos confiable que el asfalto en caliente. En este documento, se estudiará el comportamiento viscoelástico del asfalto en frío BBSG 0/10. El estudio se dividirá en dos partes: experimental y numérica.
Para la parte experimental, se realizan tres estudios principales: el módulo complejo, el comportamiento frente a la propagación de fisuras y la resistencia a la deformación permanente. Para determinar el módulo complejo, es decir, un modulo que consta de una parte real y otra imaginaria debido a las características viscoelásticas del material, se fabrican especímenes paralelepípedos y se realizan ensayos a diferentes frecuencias y temperaturas mediante el ensayo de flexión de dos puntos utilizando la máquina SYMERIS. Este ensayo permite obtener distintos tipos de curvas que, al mismo tiempo, permiten obtener distintos modelos reológicos para analizar la viscoelasticidad del material.
Para analizar el comportamiento de la propagación de fisuras, se fabrican especímenes semicirculares y a dos temperaturas, 5°C y 20°C, se realizan ensayos de flexión a 3 puntos utilizando una prensa hidráulica. El último ensayo es el de deformación permanente. Para ello, se realiza el llamado rutting test, que se basa en la aplicación de una carga rodante a 60°C durante una gran cantidad de ciclos sobre una placa de asfalto. Estos ensayos forman parte de los requisitos detallados según las normas europeas para la aprobación de un nuevo tipo de asfalto. Estas normas indican los distintos rangos de resultados que los ensayos deben tener para ser aptos y, en caso de no respetar el rango, alguna característica del asfalto debe ser cambiada.
Los resultados del módulo complejo permiten encontrar los parámetros del modelo de Maxwell Generalizado y por lo tanto estudiar numéricamente la resistencia a la propagación de fisuras. El objetivo

final de este trabajo es el de simular dicho ensayo utilizando un modelo de campo de fase para analizar la evolución de la interfase fisura-nofisura y obtener resultados similares tanto numérica como experimentalmente.

Abstract

When discussing road construction and maintenance, asphalt emerges as a frequently employed material. Historically, hot mix asphalt has been the preferred option. Nevertheless, in recent years, cold mix asphalt has gained attention due to its unique characteristics and advantages. One of the reasons is the decarbonization of the construction industry that is one of the objectives for the incoming decades. The use of cold asphalt is one of the means to achieve this goal because of his very low impact to the environment. However, their mechanical behavior at a young age, their aging and their recycling are very poorly known.

Cold asphalt is produced using bitumen emulsion, a mixture made of 35-75% of bitumen, 25-65% of water and around 1% of emulsifier, combined with aggregates. Thanks to the bitumen emulsion, the mixture can be applied and compacted at low temperatures, offering an advantage over conventional asphalt, which must be maintained at 130-180°C during paving and 150-180°C during transport. This high temperature results in significant energy consumption.

Despite its advantages, the properties and viscoelastic behavior of cold asphalt make it less reliable than hot asphalt. In this document, the viscoelastic behavior of cold BBE 0/10 asphalt will be studied. This study will be divided into two parts: experimental and numerical.

For the experimental part, three main studies are conducted: complex modulus, crack propagation and rutting test. To determine the complex modulus, parallelepiped specimens are fabricated and tested at different frequencies and temperatures using the 2-points bending test. To analyze the crack propagation behavior, semi-circular specimens are made and tested at different temperatures. Finally for the rutting test, two rectangular parallelepiped specimens are fabricated and tested at high temperature.

For the numerical part, a 2-dimensions crack growth media is simulated using the complex modulus data obtained experimentally. Then, the numerical results are compared to the SCB test results.

Introduction

About the company

The "Centre d'études et d'expertise sur les risques, l'environnement, la mobilité et l'aménagement (CEREMA) is the major French public agency for developing public expertise in the fields of urban planning, regional cohesion and ecological and energy transition for resilient and climate-neutral cities and regions. It has a staff of 2,600 people out of which 500 are dedicated to research and innovation activities. Cerema was created in 2014 by merging eleven public expertise organizations, each with decades of experience in the fields of bridges, roads and ports infrastructure, water, geotechnics, risk, land use and urban development. As a multidisciplinary scientific and technical resource and expertise center, Cerema provides assistance in developing, implementing and assessing public policies at national and local levels, where the challenges of the climatic and ecological transition and regional cohesion are paramount.

Figure 1: Logo of CEREMA

Cerema's activities are organized in 6 domains:

- ☞ Building.
- ☞ Mobility.
- ☞ Transport infrastructure.
- ☞ Environment and risk.
- ☞ Sea and coast.
- ☞ Regional expertise and engineering.

Cerema has:

- ☞ Staff of 2500 people.

- ☞ 359 M€ of budget.
- ☞ 50 ongoing European projects.
- ☞ 12 research teams.
- ☞ 3000 products in the CeremaDoc website.
- ☞ 26 sites in mainland France and overseas territories.

Figure 2: Sites of Cerema

The internship took place at Cerema Ile-de-France, Sourdun in the Infrastructures, Risks, and Materials department.

Chapter 1

Bibliographic review

This first chapter has for goal to introduce some theoretical aspects about bituminous materials, with a focus on the initial definitions of cold asphalt mixtures. Then, the main properties of the asphalt will be discussed. Additionally, various tests usually conducted to characterize bituminous materials will be explained.

1.1. General Information on bituminous asphalt

1.1.1. Definition of bituminous mixtures

A bituminous mixture is a composite material made of aggregates, hydrocarbon binder and additives. It is mainly used in civil engineering for the construction of roads particularly for pavements.

1.1.2. Components of bituminous mixtures

1.1.2.1. Aggregates

The aggregates represent the skeleton of the pavements and it represents approximately 95% of its mass. They are a key element considering they are in charge of supporting and transmitting the efforts caused by the traffic wheel loads. Aggregates can be natural, manufactured or recycled from old mixtures. Natural aggregates are generally extracted from larger rock formations through an open excavation (quarry). Extracted rock is typically reduced to usable sizes through mechanical crushing. Manufactured aggregate is often a byproduct of other manufacturing industries. Their diameters are comprehensive from 0mm to 45mm and they are divided in different classes according to their minimal (d) and maximal (D) diameters. The different classes are shown in the table 1.1.

Aggregate	**Minimum diameter (mm)**	**Maximal diameter (mm)**
Fines	0	$D \leq 0.063$
Fine aggregate	0	$D \leq 2$
Coarse aggregate	$d \leq 2$	$2 \leq D \leq 45$
All-in aggregate	0	$2 \leq D \leq 45$

Table 1.1: Classification of aggregates.

1.1.2.2. Hydrocarbon binders

The asphalt binder, made of bitumen, is an essential component of asphalt concrete as well. It is the element that holds the aggregate together. According to the European standard EN 12597 the asphalt binders can be categorized as follows:

- Paving Grade Bitumens.
- Special Paving Grade Bitumens.
- Cutback Bitumen.
- Bituminous Emulsions.
- Modified Bitumens.
- Industrial Bitumens.

The bitumen is an organic material of animal origin, obtained by distillation of petroleum. It is a black substance, solid or semi-solid, composed of hydrocarbons in colloidal form (80% carbon, 10% hydrogen, 3% nitrogen, and 2% oxygen).
The bitumen can be classified according to their penetrability at a constant temperature (see table 1.2). In order to determinate the penetrability the European norm NF EN 1426 describe a standardized test.

Grade	Bitumen type
10/20 - 15/25	Hard
20/30 - 50/70	For roads purposes
70/100 - 160/220	Soft

Table 1.2: Classification of bitumen.

1.1.2.3. Bitumen emulsion

In the case of this study, the cold bituminous mixtures are made with bitumen emulsion. The bitumen emulsion is a mix between the bitumen itself and water. Since the bitumen is an oily product and cannot mix with water, an emulsifier is added to water before mixing. The emulsifier works as a surface active agent that helps to break bitumen into minuscule droplets suspended and dispersed. The bitumen percentage is kept around 60 and the rest is water. When sprayed on the road, the water particles in the emulsion are released and evaporated, causing the bitumen to settle and harden. The time taken for setting of bitumen varies with the different grades of bitumen.

The classification of the bitumen emulsions is made depending on the percentage of bitumen found in the mix (see table 1.3) according to the standard NF EN 13808. The viscosity is other important parameter when discussing bitumen emulsions and is measured according to the standard NF EN 12846-1.

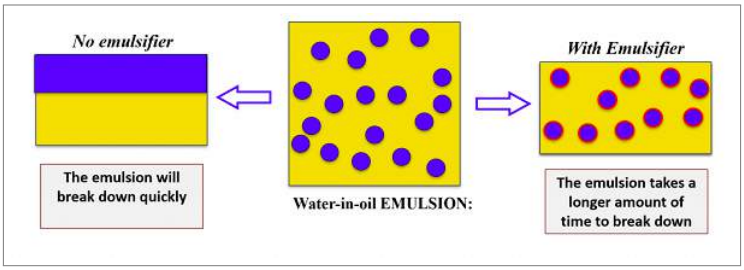

Figure 1.1: Water-oil mix with and without emulsifier.

Bitumen emulsion	Classification	Binder content [%]
Class 0	-	-
Class 1	-	-
Class 2	C35	<38
Class 3	C40	38 to 42
Class 4	C50	48 to 52
Class 5	C55	53 to 57
Class 6	C60	58 to 62
Class 7	C65	63 to 67
Class 8	C67	65 to 69
Class 9	C69	67 to 71
Class 10	C70	$\geq$ 69
Class 11	C72	$\geq$ 71

Table 1.3: Classification of bitumen emulsions.

1.1.2.4. Other components

Components not mentioned previously can also be found in pavements. For example, recycled aggregates from old pavements and additives such as polymers or rejuvenators are often included to enhance the performance and longevity of mix asphalts.

1.1.3. Characterization tests

1.1.3.1. Aggregates

The aggregates are classified according to the particle size distribution using a sieving method. This method consists, according to the standard EN 933-1, of dividing and separating a material into several particle size classifications of decreasing sizes by means of a series of sieves. The aperture sizes and the number of sieves are selected in accordance with the nature of the sample and the accuracy required. The result is presented in the form of a graph with the sieve mesh diameter on the x-axis and the cumulative percentage of sieved material on the y-axis. This characteristic is particularly important for controlling the homogeneity of the mixture.

1.1.3.2. Characterization of binders

1.1.3.2.1. Needle penetration test (NF EN 1426)

This test consist in measuring the penetration of a standard needle by application of a 100g load during 5s. For penetrations up to 330mm, the temperature has to be maintain at 25°C and for prenetations above 330mm, the temperature has to be reduced at 15°C without changing other parameters of the test. The types of bitumen are found in the table 1.2. The higher the penetrability, the softer the bitumen is.

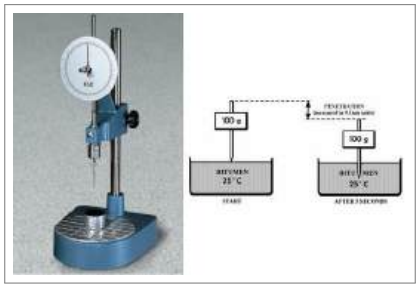

Figure 1.2: Needle penetration test.

1.1.3.2.2. Ring and Ball test (NF EN 1427)

This test allows to evaluate the behavior of bitumen under the effect of heat. Conducted under standardized conditions of temperature increase, this test consists of determining the temperature at which a ring of bitumen supporting a steel ball deforms by elongating until it reaches a marker located at a fixed distance.

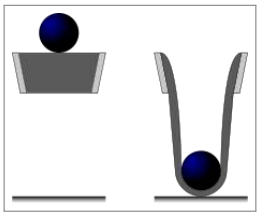

Figure 1.3: Ring and ball test.

1.1.3.2.3. Fraass breaking point test (NF EN 12593)

This test allows to describe the brittleness of bitumen at low temperatures. A sample of bituminous binder is applied to a metal plate at an even thickness. This plate is subjected to a constant cooling rate and flexed repeatedly until the binder layer breaks; the temperature at which the first crack appears is reported as the Fraass breaking point.

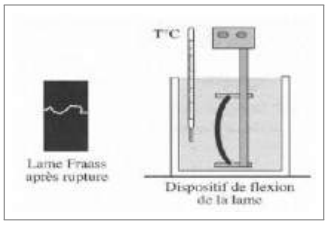

Figure 1.4: Fraass breaking point device.

1.2. Pavement structure

1.2.1. Definition

The pavement can be described as the surface where the vehicles travel. It consists of different components and layers. Its main function is to distribute the applied vehicular loads to the underneath layers.
The different components of the road structure are (figure 1.5):

1. Subgrade.
2. Sub-base Course.
3. Base course.
4. Surface course or wearing course.

Subgrade: It is defined as the finished and compacted surface of earthwork on which a road pavement rests. The subgrade of a road may be provided on an embankment, in cutting or existing ground level depending upon the topography and the finalized formation level. It consists of well compacted natural soil brought to the required camber and gradient.

Sub-base: It is a layer of granular material provided in between the subgrade and the base course. The sub-base is provided as an additional layer when the subgrade is of poor quality. It consists of a layer of comparatively cheaper material like burnt clinker, natural gravel, or slag.

Base course: This course is considered as the most important and major component of road structure because this course is to bear the impact of traffic transferred through the wearing course. It consists of a stable material like boulders, gravel, one or two layers of well-burnt bricks, etc. In case of rocky subgrade, this course is not provided.

Surface course: It is the topmost layer of the road pavement directly exposed to traffic. A good surface course should be impervious and weather resisting. it should be able to resist the abrasive action of the traffic.

1.2.2. Types of asphalt

When talking about asphalt, a simple classification according to the company SUPERIOR ASPHALT, LC. is as follows:

Hot mix asphalt (HMA): Hot asphalt is the most used type of asphalt. It is made by heating a mixture of aggregate (crushed stone, gravel, and sand) and hydrocarbon binder at a high temperature,

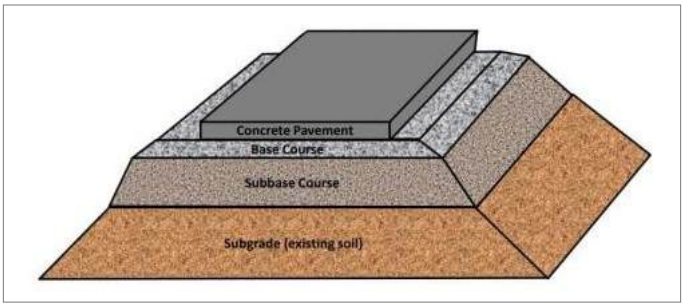

Figure 1.5: Pavement structure.

usually around 150-180 degrees Celsius. The mixture is then mixed and transported to the job site, where it is laid and compacted while still hot.

Warm mix asphalt (WMA): Warm asphalt mix is a relatively new type of asphalt that is made at a lower temperature than HMA, typically between 90-120 degrees Celius. This type of asphalt can be produced using various methods, including foaming, emulsion, and chemical sealer additives and it can be used in the same applications as hot mix asphalt, such as roads, highways, and airports, but also for low-volume projects such as driveways and parking lots.

Cold mix asphalt (CMA): Cold mix asphalt is mixed and applied at lower temperatures than hot and warm asphalt. It is typically mixed at temperatures between -15°C and 20°C. This asphalt is typically made by combining aggregate, bitumen emulsion, and a small amount of water, creating a workable mixture that can be applied to the road's surface. It is then compacted and left to cure, forming an asphalt surface.

Ultra-thin pavement(UPM): Ultra-Thin Pavement is a type of asphalt designed for very thin layers, typically between 3-8 centimeters thick. They're also called "Fines", which are used for repairing low spots, so the edge can match with the existing pavement. This type of asphalt uses a high-performance binder and a specially designed aggregate blend to produce a durable, long-lasting surface. UPM is often used where traditional asphalt is not an option, such as over existing asphalt or concrete surfaces or where the existing subgrade is unsuitable for conventional asphalt. UPM is also a good option for locations with weight restrictions, such as bridges.

Porous asphalt: Porous asphalt is a type of asphalt that is designed to allow water to pass through the surface, reducing the risk of flooding and erosion. It is made using a unique blend of aggregates and asphalt binder that creates small voids or pores in the surface, allowing water to filter through to the subgrade.

Dense-graded mixes: Dense-graded asphalt is a type of asphalt that is characterized by its high density and uniformity of aggregate size. It combines a precise blend of coarse and fine aggregates and asphalt cement to create a durable and long-lasting surface. This mixes are often used for constructing roads, highways, airports, high-traffic areas, parking lots, driveways, and other low-volume projects. It also can be used as a base course for different types of asphalt surfaces.

Choosing the right asphalt depends on various factors including location, climate, traffic volume, and budget.

1.2.3. Cold mix asphalts

Cold mix asphalt, as already seen, is an asphalt mixture that can be produced and applied at ambient temperatures. Unlike hot mix asphalt, which requires high temperatures for production

and placement, cold mix asphalt can be used without the need of heating. This makes it a versatile and convenient option for various applications, especially in situations where hot mix asphalt is not readily available or practical.
Advantages of cold mix asphalt:

- **Versatility**: Cold mix asphalt can be used in various weather conditions and temperatures, making it a flexible solution for road repairs and maintenance.
- **Cost-Effective**: Cold mix asphalt typically requires fewer resources and equipment compared to hot mix asphalt. It can be produced on-site, reducing transportation costs and the need for specialized machinery.
- **Convenience**: Since cold mix asphalt can be applied at ambient temperatures, it eliminates the need for heating equipment, allowing for faster and more efficient repairs.
- **Durability**: With the use of additives and specialized emulsions, cold mix asphalt can offer excellent durability and resistance to cracking and deformation.
- **Extended Workability**: Cold mix asphalt has an extended workability period, providing more time for placement and compaction, especially in remote or challenging locations.

Despite the advantages offered by cold asphalt, it is not commonly used for the construction of highways or long roads. However, there are several practical applications for this type of asphalt, including:

- **Pothole Repairs**: Cold mix asphalt is commonly used for pothole repairs, offering a quick and effective solution to restore damaged road surfaces.
- **Emergency Repairs**: In emergency situations where immediate repairs are needed, cold mix asphalt can be applied without delay, ensuring the safety of motorists and pedestrians.
- **Temporary Pavements**: Cold mix asphalt can be used to create temporary pavements for construction zones, events, or detours, providing a smooth and safe surface for temporary traffic.
- **Remote Locations**: It is particularly useful in remote or hard-to-reach locations where hot mix asphalt plants may not be readily available.
- **Low-Volume Roads**: For low-traffic volume roads, cold mix asphalt can be a cost-effective and durable solution for surfacing and maintenance.

1.2.4. Pavement loads

The road pavements are usually affected by two main different loads, the loads produced by the traffic and the loads produced by the temperature variations.

1.2.4.1. Traffic effect

The loads produced by the circulations of the vehicles are seen as compression forces on the upper layers and traction forces on the lower layers.

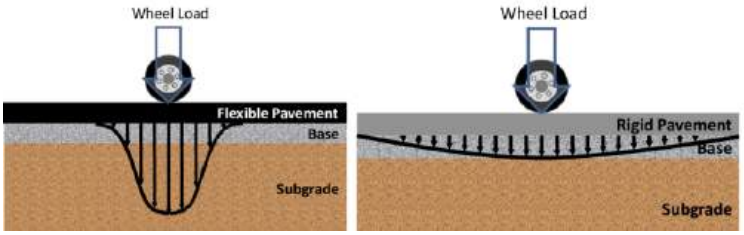

Figure 1.6: Traffic load.

1.2.4.2. Thermal effect

The different temperatures cause effects of expansion and retraction. These effects produce residual stresses and strains that produce the damage of the pavement.

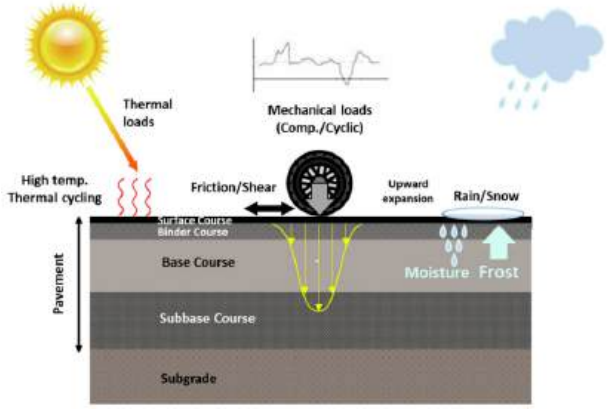

Figure 1.7: Environmental effect on pavement (Al-Atroush, 2022).

1.2.4.3. Other effects

Other situations can cause the damage of the pavement as well. One example is the effect of the water that can produce moisture damage.

1.3. Mechanic behavior of pavements

Di Benedetto describes four behavior domains of bituminous mixtures (Di Benedetto and Corté, 2004) considering the load cycle number and the level of deformation. These domains are:

- Linear viscoelastic behavior.
- Non-linear viscoelastic behavior.
- Thermal viscoplastic behavior.
- Fatigue behavior.

The linear viscoelastic domain will be studied in this work.

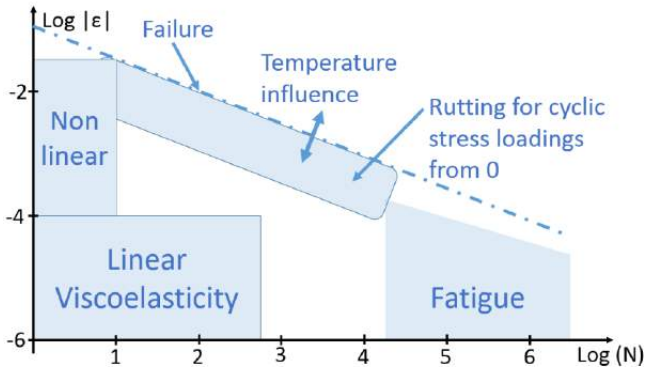

Figure 1.8: Asphalt behavior at fixed temperature (Di Benedetto and Corté, 2004).

1.3.1. Linear viscoelastic behavior of asphalts

In order to evaluate the properties and performance of the bituminous mixtures, various tests are made. One key test is the stiffness test, which allows us to determine the complex modulus of the material. Since a viscoelastic material is studied, this stiffness depends on temperature and load speed. Another test performed is the crack propagation test, which enables to determine the fracture toughness of the sample.

1.3.1.1. Characterization of behavior in the frequency domain

1.3.1.1.1. Complex modulus test

The aim of this test is to determinate the complex modulus in the linear viscoelastic domain. Different types of specimens can be used, such as, trapezoidal, parallelepiped and cylindrical. The modulus and the phase angle between the real and imaginary part is obtained as a result of the test. For conducting the test, a sinusoidal strain of amplitude ε_0 with a pulse ω is applied.

$$\varepsilon^*(t,\omega) = \varepsilon_0 sin(\omega t) \tag{1}$$

Then, a stress as response is obtained:

$$\sigma^*(t,\omega) = \omega_0 sin(\omega t + \delta) \tag{2}$$

Thus, the complex modulus is defined as the relation between the strain and the stress.

$$E^*(\omega) = \frac{\sigma^*(t,\omega)}{\varepsilon^*(t,\omega)} = E_1 + jE_2 = |E^*|e^{j\omega t} \tag{3}$$

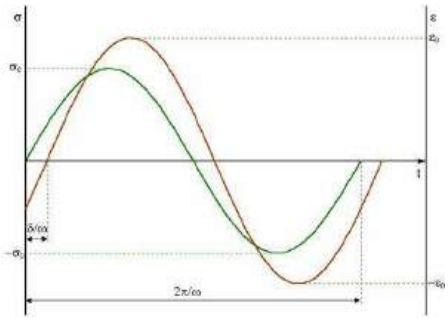

Figure 1.9: Stress-strain delay.

For elastic materials, the phase angle is equal to zero, so the complex modulus is equal to the Young's modulus. In low-temperature conditions for asphalt mixtures, this scenario can occur, where the complex modulus is denoted as E_∞.

1.3.1.1.2. Results of the complex modulus test

The properties of materials are closely tied to temperature and loading speed. Various representations are employed to analyze the results of the stiffness test.

Isotherm and isochronal curves

The isotherm curves (figure 1.10a) depict the complex modulus in graphics generated at the same temperature but varying frequencies. Conversely, the isochrone curves (1.10b) illustrate the complex modulus at a consistent frequency as a function of temperature.

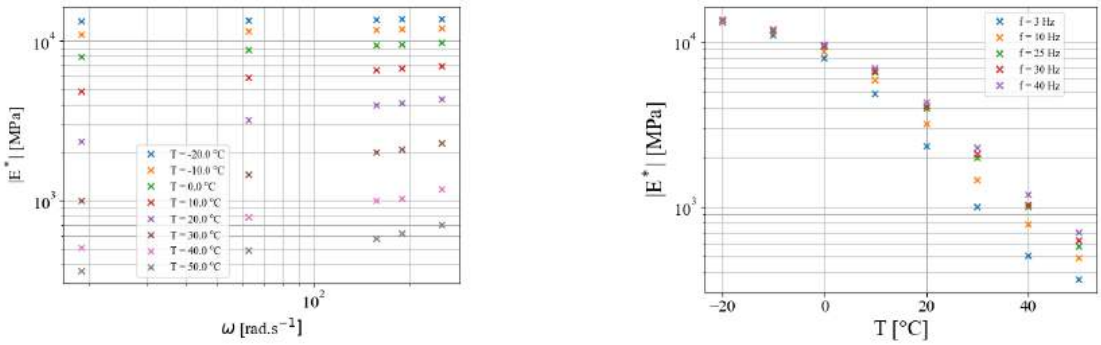

(a) Isothermal of the modulus magnitude.

(b) Isochrone of the modulus magnitude.

Figure 1.10: Typical isothermal and isochrone graphics.

Black and Cole-Cole curves

The graph Cole-Cole (figure 1.11b) illustrate the real part of the modulus as a function of the imaginary part. The black curve (figure 1.11a) represents the norm of the complex modulus as a function of the phase angle.

1.3.1.1.3. Master curves

The master curve is a graphical representation illustrating the complex modulus at different frequencies but at the same temperature. It is derived from the combination of results obtained through

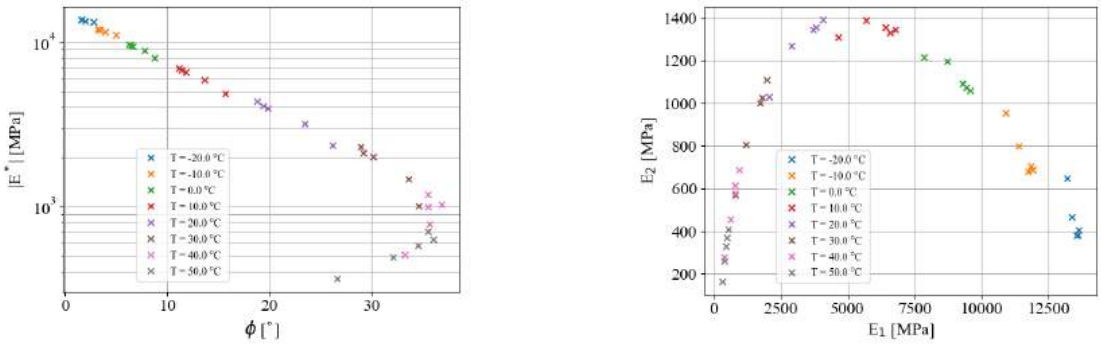

(a) Black diagram.

(b) Cole-Cole diagram.

Figure 1.11: Complex modulus in Cole-Cole and black diagrams.

complex modulus testing. By utilizing data from various temperatures, an interpolation can be done to determine the modulus at a reference temperature but with a different frequency.
Kramers-Kronig relations (Chailleux et al., 2006) give the following equations:

$$log|E^*(\omega)| - log|E^*(\infty)| = -\frac{2}{\pi}\int_0^\infty \frac{u.\delta(u) - \omega.\delta(\omega)}{u^2 - \omega^2}du \tag{4}$$

$$\delta(\omega) = \frac{2\omega}{\pi}\int_0^\infty \frac{log|E^*(u)| - log|E^*(\omega)|}{u^2 - \omega^2}du \tag{5}$$

According to different experimental results Booij and Thoone (Booij and Thoone, 1982) proposed the following relation:

$$\delta(\omega) = \frac{\pi}{2}\frac{dlog(|E^*(\omega)|)}{dlog(\omega)} \tag{6}$$

If two close frequencies ω_i and ω_j are considered, the relationship (6) can be written as:

$$\delta_{avr}^{(\omega_i,\omega_j)}\frac{2}{\pi} = \frac{log(|E^*(T,\omega_j)|) - log(|E^*(T,\omega_i)|)}{log(\omega_j) - log(\omega_i)} \tag{7}$$

Where $\delta_{avr}^{(\omega_i,\omega_j)}$ is the average of two angles measured at ω_i and ω_j (for temperature T).
If the time-temperature equivalency principle can be applied, a shift factor exists $a_{(T_1,T_2)} = \omega_1/\omega_2$ such as $log(|E^*(T_1,\omega_1)|) = log(|E^*(T_2,\omega_2)|)$. Thus, for two close frequencies the relationship (7) can be written :

$$\delta_{avr}^{(T_1,T_2)}(\omega_2).\frac{2}{\pi} = \frac{log(|E^*(T_1,\omega_2)|) - log(|E^*(T_2,\omega_2)|)}{log(a_{(T_1,T_2)})} \tag{8}$$

Where $\delta_{avr}^{(T_1,T_2)}$ is the average of two angles measured at T_1 and T_2 (for ω_2). Therefore, shift factors can be calculated using equation (8) for close isotherms at only one frequency.
Considering the experiments are carried out at temperature T_1, T_2, ..., T_i, T_{i+1}, ..., T_n, master curve can be crated related to a reference temperature (T_{ref}). Hence, shift factor, needed to be applied for an isotherm T_i according the reference temperature T_{ref} can be calculated as:

$$log(a_{(T_i,T_{ref})}) = \sum_{j=1}^{j=ref}\frac{log(|E^*(T_j,\omega)|) - log(|E^*(T_{j+1},\omega)|)}{\delta_{avr}^{(T_j,T_{j+1})}(\omega)}\frac{\pi}{2} \tag{9}$$

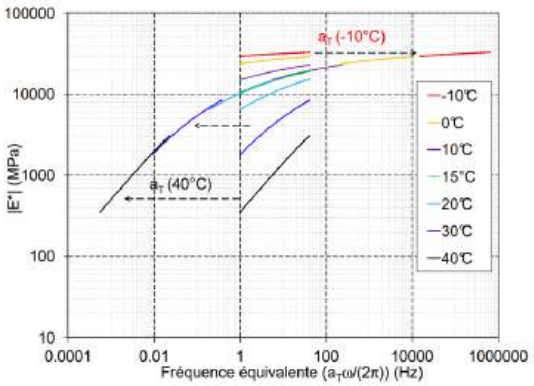

Figure 1.12: Construction of master curves.

1.3.2. Characterization of viscoealstic behavior: Rheological models

1.3.2.1. Introduction

Rheology is the science of flow and deformation of matter and describes the interrelation between force, deformation and time. Rheology is applicable to all materials, from gases to solids. Fluid rheology is used to describe the consistency of different products, normally by the two components viscosity and elasticity. By viscosity is usually meant resistance to flow or thickness and by elasticity usually stickiness or structure.
Rheological models are often used to exemplify the structure of phenomenological material models. For this purpose, different elements, representing elastic, viscous or plastic material behaviour, are combined in parallel and series connections.
The components that can be found in the different models are:

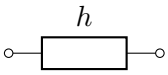

(a) Parabolic element.

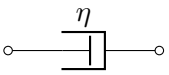

(b) Viscous element.

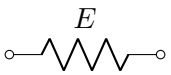

(c) Elastic element.

Figure 1.13: Components used for describing viscoelastic behavior of materials.

1.3.2.2. Maxwell model

The Maxwell model is represented by a purely viscous damper and a purely elastic spring connected in series.

The equation of the system is:

$$\sigma + \frac{\eta}{E}\dot{\sigma} = \dot{\varepsilon} \tag{10}$$

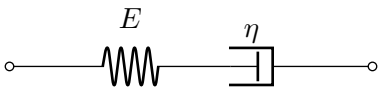

Figure 1.14: Maxwell model.

1.3.2.3. Kelvin-Voigt model

The Kelvin-Voigt model is also represented by a spring and a damper, but in this case they are in paralel.

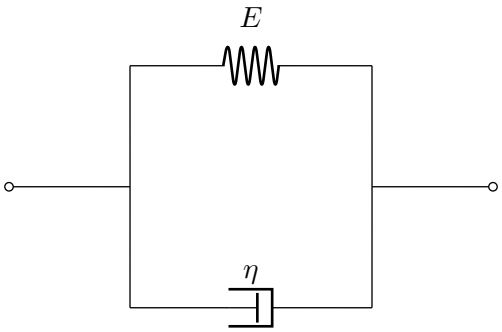

Figure 1.15: Kelvin-Voigt model.

In this case, the equation of the system results:

$$\sigma = E\varepsilon + \eta\dot{\varepsilon} \tag{11}$$

1.3.2.4. Generalized Maxwell model

This model consist in n Maxwell model connected in parallel. An extra isolated spring is also added in parallel to represent the final (or equilibrium) modulus. In the maxwell model there is only one relaxation time that is constant. However, this does not wholly simulate the viscoelastic behavior of most materials. For this reason, the generalized Maxwell model is commonly applied since it has n relaxation times.

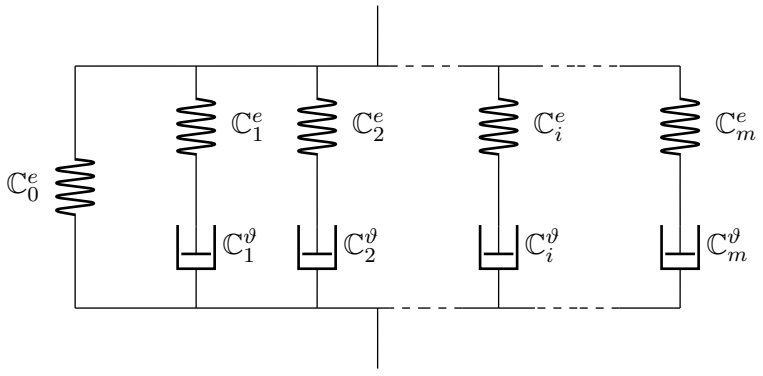

Figure 1.16: Generalized Maxwell model (GM)

The relaxation time is calculated as:

$$R(t) = E_0 + \sum_{i=1}^{n} E_i exp\left(-\frac{t}{\tau_i}\right) \tag{12}$$

And the equation of the complex modulus is:

$$E^*(\omega) = E_0 + \sum_{i=1}^{n}\left(E_i \frac{j\omega\tau_i}{1 + j\omega\tau_i}\right) \tag{13}$$

1.3.2.5. Huet Sayegh model

The Huet-Sayegh model (figure 1.17), proposed in 1965 (Sayegh, 1966), is a modification of the Huet model that consists of two parabolic creep elements connected in series with a spring. The original Huet model represented the behavior of binders, while Sayegh's modification that involved adding a low-stiffness spring (E_0) in parallel with the Huet model allowed to model the behavior of bituminous asphalt even at low frequencies.

The complex modulus of this model can be calculated as follows:

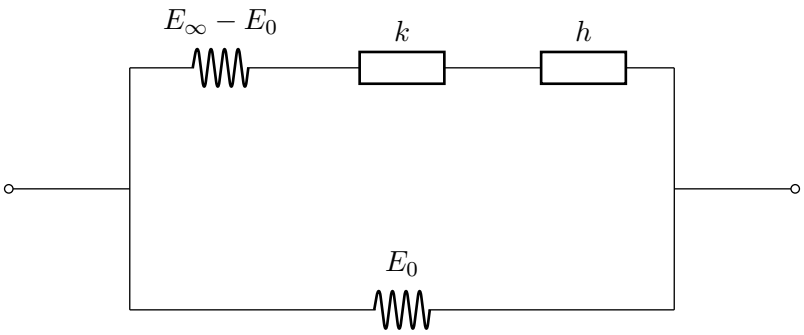

Figure 1.17: Huet-Sayegh model.

$$E^*(\omega) = E_0 + \frac{E_\infty - E_0}{1 + \delta(j\omega\tau)^{-k} + (j\omega\tau)^{-h}} \tag{14}$$

1.3.2.6. 2S2P1D model

The 2S2P1D (Olard and Benedetto, 2003) is a rheological model very often used to curve-fit the linear viscoelastic properties for bitumens and asphalt mixtures. It consists of combinations of two springs, two parabolic creep elements and one dashpot where each component plays an important role when describing the viscoelastic behavior. The model representation can be shown in figure 1.18 and the role of each component in the figure 1.19.

The complex modulus can be calculated as:

$$E^*(\omega) = E_\infty + \frac{E_0 - E_\infty}{1 + \delta(j\omega\tau)^{-k} + (j\omega\tau)^{-h} + (j\omega\beta\tau)^{-1}} \tag{15}$$

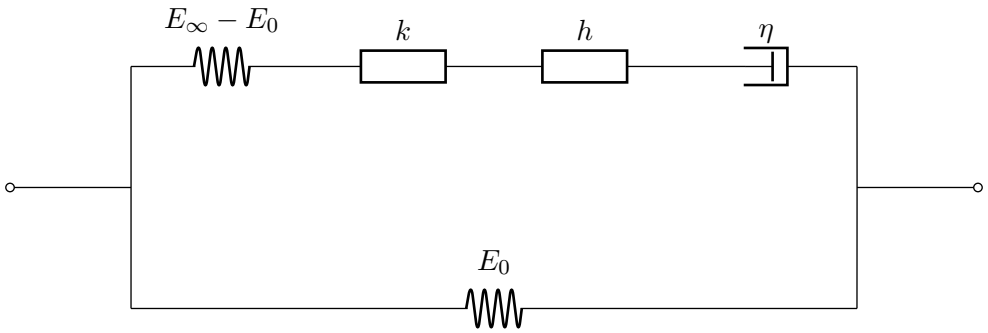

Figure 1.18: 2S2P1D model.

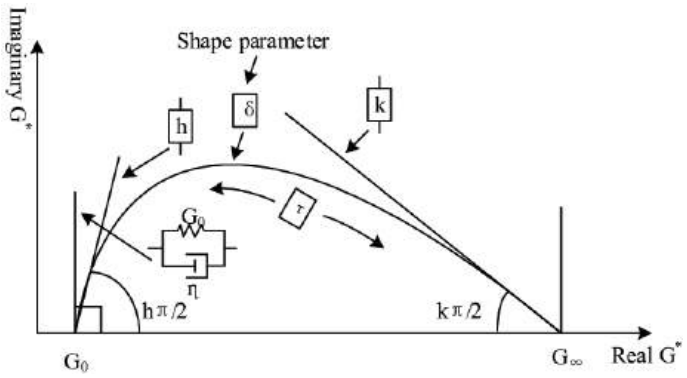

Figure 1.19: Cole-Cole graphic for 2S2P1D model (Riccardi et al., 2017).

1.4. Cracking tests

1.4.1. Fracture mechanics

The fracture mechanics is the field of mechanics concerned with the study of the propagation of cracks in materials. It was first introduced by Griffith in 1920 (Griffith, 1920). It is based in characterizing the behavior of the cracks by using different engineering parameters such as stress field, crack size and crack resistance of the material.
The hypothesis of this theory are the following:

- The material is non-homogeneous (continuous medium) with elastic, linear, and isotropic behavior;
- The crack is planar and has a straight front.

According to this theory, there are 3 main fracture modes (see figure 1.20). The mode I is an in-plane opening, which is the most common case, mode II is an in-plane shear, and mode III is an out-of-plane shear loading. A combination of two modes is normally named "mixed mode".
Various authors such as Li and Marasteanu (2010), Aliha et al. (2015) and Kim and El Hussein (1997) have studied the behavior of asphalt mixtures using fracture mechanics. Most of these studies focus on mode I while mode II has not been extensively investigated despite its presence in real-world conditions. The mixed mode (I-II) has also been studied and one of the conclusions is that the most damaging mode for pavements is the mixed mode.

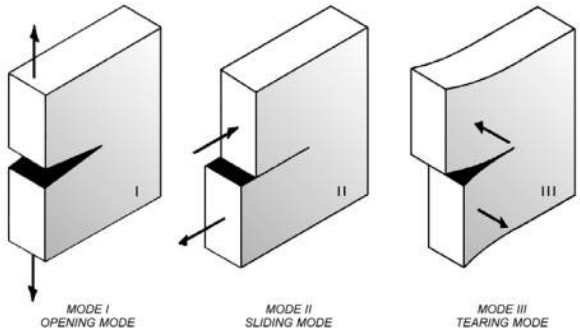

Figure 1.20: Fracture modes (Janssen et al., 2004).

Measurements and observations show that there is no regular propagation of cracks in a plane. The propagation process in bituminous asphalt can be due to three phenomena:

- Propagation within the bituminous mastic;
- Propagation at the interface between the aggregates and the binder;
- Propagation within the aggregates.

Different tests of crack propagation with different geometries (figure 1.21) are found in the literature to study the cracking behavior of bituminous mixtures. The most common tests are:

- Semi-Circular Bending test (SCB) (Krans et al., 1996);
- Single-Edge Notched Beam (SENB) (Gao et al., 2015);
- Indirect Tensile Test (ITS) (Kim and Wen, 2002);
- Disc-shaped Compact Tension (DCT) (Wagoner et al., 2005).

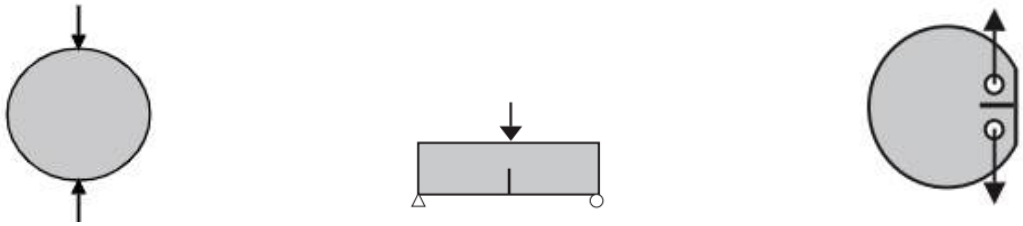

(a) Cylindrical specimen. (b) Prismatic specimen. (c) Truncated cylindrical specimen.

Figure 1.21: Different geometries for fracture tests.

1.4.2. Semi-Circular Bending Test (SCB)

This is the only European standard regarding to the fracture test. It was first introduced by Chang and Kuruppu (Chong and Kuruppu, 1984) and it consists of applying a 3-point bending load to a semi-circular specimen. The specimen has a small crack on the bottom face to accelerate the process. This test allows us to obtain a Force-Displacement curve. We can vary the speed of the applied force and the temperature of the specimen to analyze their influence.
The placement of the supports can be changed in order to test the mode I and the mixed mode (mode I-II). The main advantage of this test is the ease of obtaining the specimens. Using a PCG machine, the asphalt can be easily cut to create the semi-circular specimens. Additionally, a significant number of specimens can be fabricated in a short time. However, this method also has the disadvantage of producing small specimens, which result in a limited rupture surface and high pressure on the top of the specimen due to the geometry, causing the crack to propagate in this zone.

(a) Mode 1 disposition. (b) Mixed mode disposition.

Figure 1.22: SCB specimen disposition.

The maximum stress at failure for this test is calculated as following:

$$\sigma_{max} = \frac{F_{max}}{Dt}\left[\frac{N}{mm^2}\right] \tag{1}$$

Where F_{max} represents the maximal force during testing and D and t represent the diameter and thickness of the specimen. Additionally, the fracture toughness is calculated as:

$$K_I = \sigma_{max} f(\frac{a}{W})\sqrt{\pi a}\left[\frac{N}{mm^{1.5}}\right] \tag{2}$$

Where a represents the notch depth of the specimen and $f(\frac{a}{W})$ the stress intensity factor depending on the notch depth (a) and the radius of height (W).
In the literature, there are several equations for stress intensity factors (SIF). In this case we use the equation given by the standard NF EN 12697-44:

$$f(\frac{a}{W}) = 4.782 - 1.219(\frac{a}{W}) + 0.063exp\Big(7.045(\frac{a}{W})\Big) \tag{3}$$

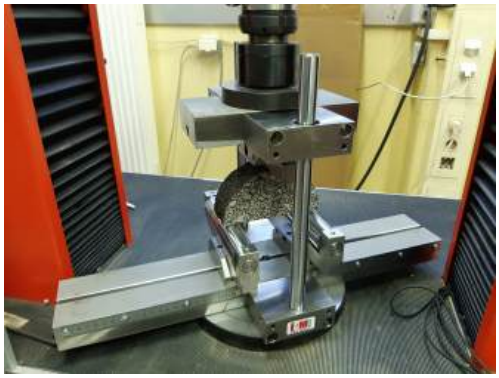

Figure 1.23: 3-points bending test machine.

1.5. Rutting test

Rutting (figure 1.24a) is one of the most common distresses in early damage to asphalt pavements. It can raise the risk of ride safety issues, accelerate pavement deterioration, and increase maintenance costs.

(a) Rutting damage.

(b) Rutting test machine.

Figure 1.24: Rutting characterization.

The rutting test goal is to analyse the permanent deformation of the asphalt surfaces that is accumulated in the wheel-paths due to the traffic loading cycles. For that, the rutting in parallelepipedal specimens is analyzed. To perform this analysis, a wheel tracking device is used (figure 1.24b) which consists of two loaded wheels that move back and forth across the surface of the asphalt specimens fixed on a table. The rolling load applied to the specimen to simulate the pressure exerted by vehicle tires is 5000 N. The test is conducted at 60°C and the specimens have to be conditioned at this temperature for 12 to 18 hours before being tested.
The test concludes when a specific number of cycles is completed or when the average rut depth reaches 20 mm. This depth is measured at different points according to the standard NF EN 12697-22+A1.

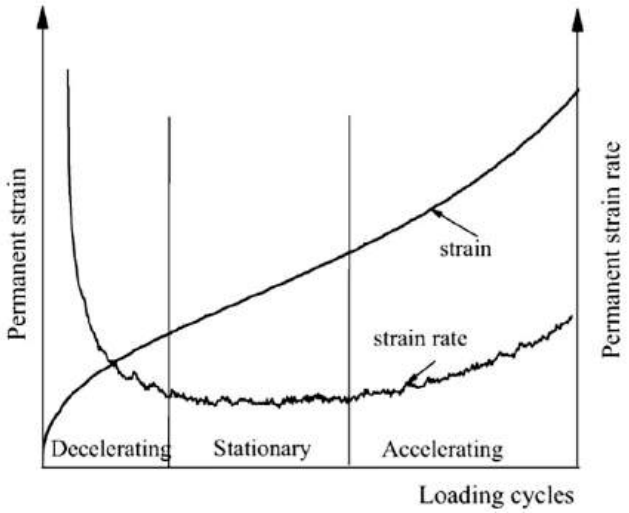

Figure 1.25: Theorical plot of accumulated permanent strain versus number of loading cycles. (Witczak et al., 2002).

1.6. Previous research on the study of cracking on asphalt

1.6.1. Study of effect of the temperature

The effects of temperature on cracking have been studied in several works. Examples often cited in the literature are Li and Marasteanu (2010) for mode I and Aliha et al. (2015) for mixed modes I/II and II.

Li and Marasteanu (2010) conducted a study on six different mixes and demonstrated that they exhibited the same behavioral change with temperature, as shown in the figure 1.26. At higher low temperatures, asphalt mixtures are more ductile and have lower peak loads and larger displacements. At the lowest temperature, mixtures are brittle and have high peak loads, and small deformation ability. At the middle low temperature, mixtures exhibited an intermediate behavior. Kim and El Hussein (1997) studied the influence of temperature on fracture toughness, focusing specifically on mode I conditions. The study was conducted over a temperature range from -5°C to -30°C in 5°C increments. The results demonstrated that toughness increased as the temperature decreased, but beyond a certain lower temperature threshold, the toughness began to decrease. This can be seen in the figure 1.27. This effect could be explained by the effect of thermal contraction. While passing from -5°C to -15°C, the contraction is increased causing an increased cohesion between aggregate and asphalt matrix, resulting and improved bonding. Below -15°C the fracture toughness decreased and this might be explained by the damage caused by the large difference in coefficients of thermal contractions between the elements of the asphalt.

1.6.2. Study of effect of the type of binder

Li and Marasteanu (2010) studied the influence of bitumen on peak load and fracture energy. They conducted experiments at three different temperatures using two types of bitumen: 50/70 and 70/100. As discussed in section 1.1.2.2, bitumen 70/100 is softer, which may explain the results shown in figure 1.28. In this figure, bitumen 50/70 (denoted as 64:P:4:G) exhibited a higher peak load but a

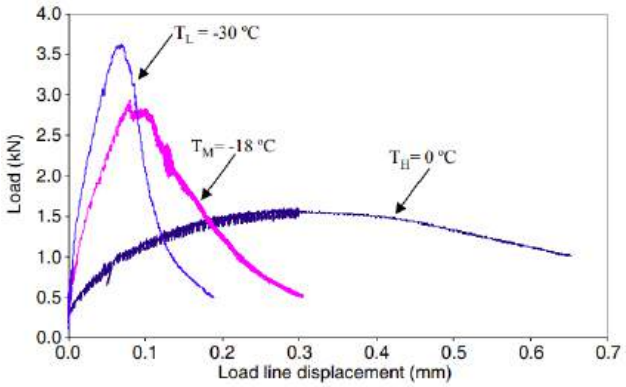

Figure 1.26: Effect of temperature on load-displacement (Li and Marasteanu, 2010).

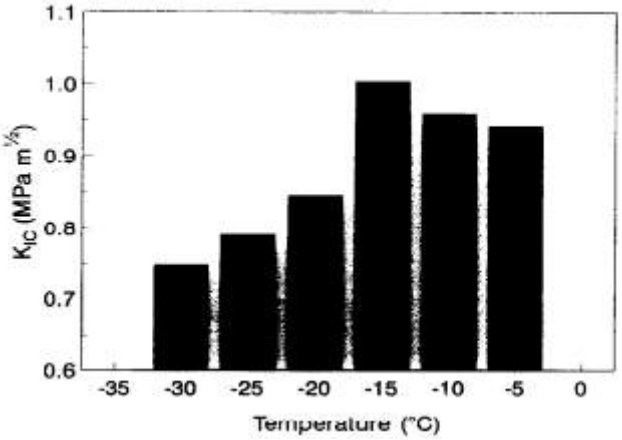

Figure 1.27: Effect of low temperature on fracture toughness (Kim and El Hussein, 1997).

lower fracture energy. Finally, considering that fracture resistance is determined not only by material stiffness but also by its ability to deform, Li and Marasteanu (2010) concluded that mixtures with 70/100 binder are more resistant to cracking than those with 50/70 binder.

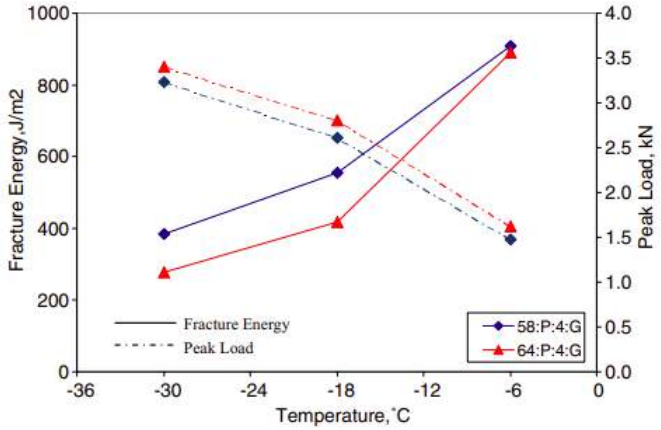

Figure 1.28: Effect of bitumen type on fracture energy and peak load (Li and Marasteanu, 2010).

1.6.3. Study of effect of different components

Imaninasab et al. (2022) studied the effects of adding RAP (reclaimed asphalt pavement) with two different agings into the bituminous asphalt. They concluded that there is no significant change between total fracture energy of short- and long-term (ST and LT) aged samples. On the other hand, embrittlement evolution by aging advancement makes asphalt mixtures more susceptible to cracking. Consequently, a mixture of 100% RAP has the least fracture energy, showing the least cracking resistance. At the same time, 73%, 65% and 57% RAP have similar cracking resistance (figure 1.29).

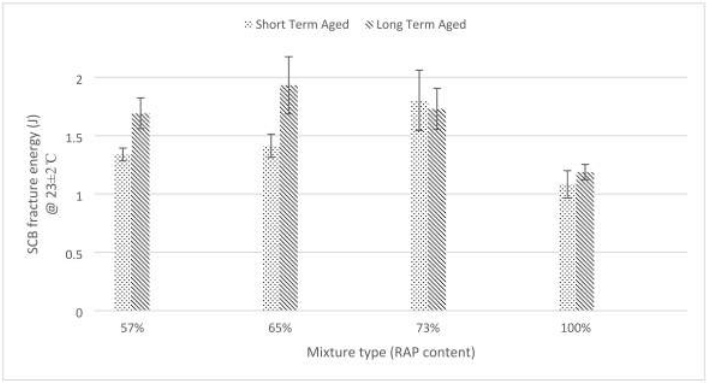

Figure 1.29: Effect of RAP content on fracture energy (Imaninasab et al., 2022).

Several authors have studied the behavior of cold asphalt modified by adding different materials. Zhang et al. (2020a) investigated the effects of incorporating mineral powder and basalt fibers. Adding mineral powder was found to improve the strength of the mixture, with results indicating that as the mineral powder content increased, the fracture energy of the mixture also increased (see figure 1.30a). However, the author recommended a content of 2-3% because a higher percentage caused some test samples to fall off from the test mold. Regarding fiber content, Zhang et al. (2020a) experimented with 6 mm and 12 mm lengths of basalt fibers. The inclusion of these fibers resulted in an increase in fracture energy due to the uniformly dispersed fibers bridging each other and forming a spatial network system within the asphalt. These fibers also limited the displacement of the aggregates, thereby restricting the failure of the asphalt. Finally, when cracks formed, fibers across the two ends of the cracks constrained their deformation and hindered the continued development of the cracks.

Al-Mohammedawi and Mollenhauer (2024) studied the influence of different type of fillers such as cement (CE), ettringite (ET), ladle slag (SD), silicafume (SF) and geopolymer (GE). He maintained the same percentage of filler and tested 3 specimens of each. He concluded that the filler changed the behavior of the material, from ductile to brittleness. Adding the cement increased the peak load but reduced the displacement until fracture while the geopolymer had the opposite effect (figure 1.31a). At the same time, the asphalt gave the lower fracture resistance while the geopolymer the higher one (figure 1.31b).

1.7. Previous research on the study of rutting on asphalt

Several authors such as Pan et al. (2023) and Xu et al. (2021) have studied the rutting on the asphalt and different factors affecting its resistance.

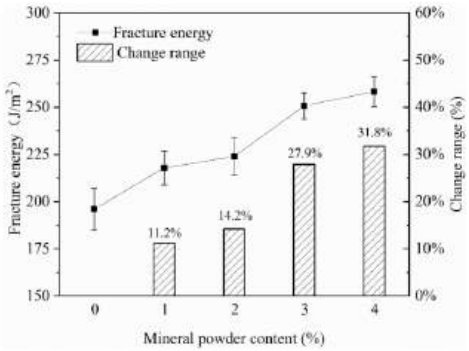

(a) Powder influence on fracture energy.

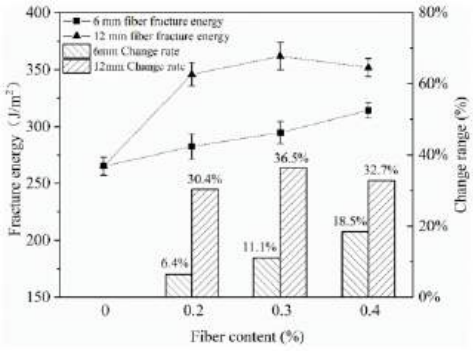

(b) Basalt fiber influence on fracture energy.

Figure 1.30: Modified cold asphalt study (Zhang et al., 2020a).

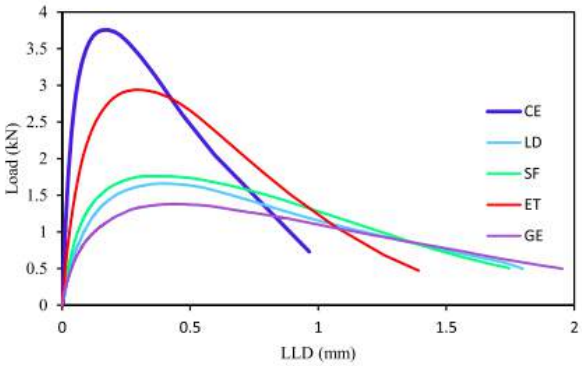

(a) Filler type effect on load-displacement.

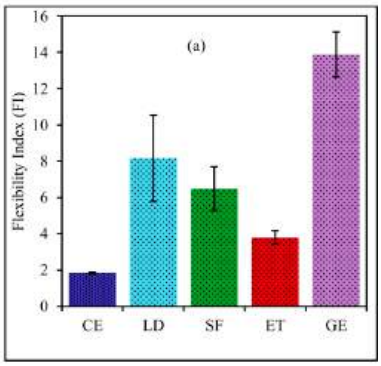

(b) Filler type effect on fracture resistance.

Figure 1.31: Filler effect on cold asphalt mixes (Al-Mohammedawi and Mollenhauer, 2024).

Pan et al. (2023) studied the effects of temperature, layer thickness, and traffic loading on asphalts with different aggregate gradation. To conduct the study, they focused on two main factors: rutting depth (RD) and dynamic stability (DS), with the latter calculated using the RD values at loading times of 45 minutes and 60 minutes. Their findings concluded that as temperature, traffic load, and the thickness of the asphalt mixture layer increase, the rutting depth increases correspondingly (see figure 1.32), while dynamic stability decreases.

Xu et al. (2021) studied the rutting effect on cold asphalt mixtures under varying temperatures and loading conditions. Their conclusions were consistent with previous studies: as temperature and traffic load increase, dynamic stability decreases (see figure 1.33).

Conclusions:

Throughout this chapter, different types of bituminous asphalt have been discussed. Also, their main characteristics have been detailed and various degradation phenomena such as cracking and rutting have been introduced. Additionally, most of the common tests for evaluating these phenomena and key bibliographic findings related to toughness and rutting have been evaluated. These discussions establish a foundational framework for this study and provide a comprehensive understanding of the elements that will be introduced in the following chapters. The next chapters are dedicated to detailing

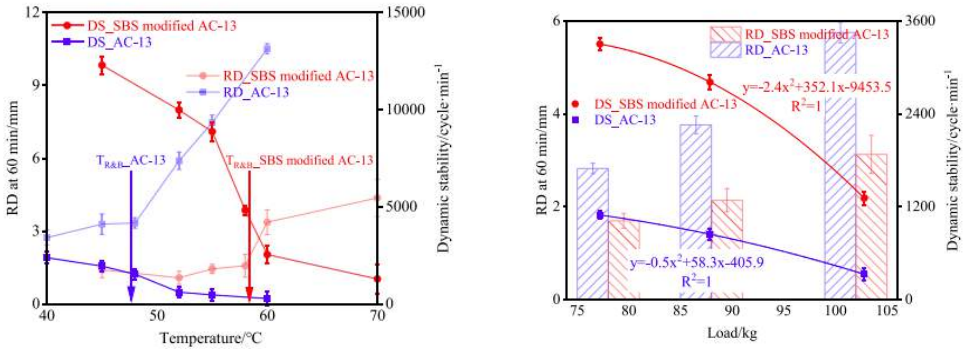

Figure 1.32: Influence of different factors on rutting (Pan et al., 2023).

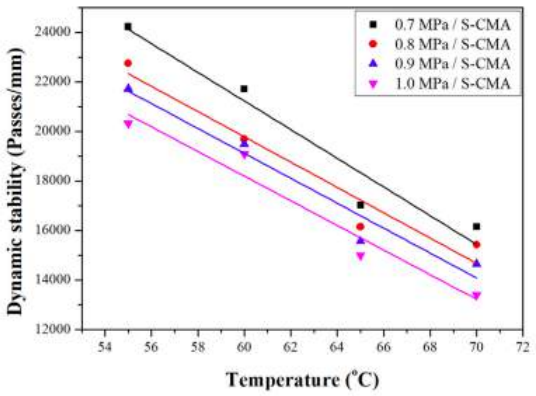

Figure 1.33: Rutting for different temperatures and loads (Xu et al., 2021).

the experimental approach, presenting the experimental results obtained and modeling the SCB test using the GetFEM library.

Chapter 2

Experimental study

Introduction

The hot asphalt and its behavior have been widely studied over the last few decades all over the world. However, cold asphalt is relatively new and, despite its advantages, its mechanic behavior has not been extensively investigated. This experimental part has for goal:

- Show the procedures involved in the fabrication of cold asphalt;
- Study the viscoelastic behavior and the mechanic performance as well as the influence of different factors.

To achieve this, first the materials used are presented. Next, the various steps in the fabrication of the specimens are detailed. Finally, the different tests and their operating procedures are discussed at the end of the chapter.

2.1. Fabrication of specimens

The cold pavement named BBE (Béton Bitumineux à l'émulsion in French) 0/10 is studied. This type of asphalt is normally used as surface course with 4 to 7 cm of thickness. The production of this asphalt concrete has been made in laboratory by the mixing of aggregates, water and bitumen emulsion.

2.1.1. Asphalt concrete composition

2.1.1.1. Aggregates

The initial step in the fabrication of bituminous mixture specimens involves conducting the grading analysis. The classification of the aggregates is determined by their respective sizes, as discussed in section 1.1.
The BBSG (Béton Bitumineux Semi-Grenu in French) 0/10 mixture is employed, where the maximum size of the aggregates is 10 mm and the minimum is 0 mm. We test 3000 g of material using the percentages listed in table 1.1.

Fraction of aggregate	Mass content [%]
0/2	26.10
2/6.3	24.3
6.3/10	41.4
Filler	2.8

Table 2.1: Composition of the bituminous mixture.

Different sieves and a weight balance are used for calculating the passing mass for the different aggregate sizes. The results can be seen in the figure 2.1. We can see that the result is similar to the theoretical data, so we keep the same percentage of aggregates.

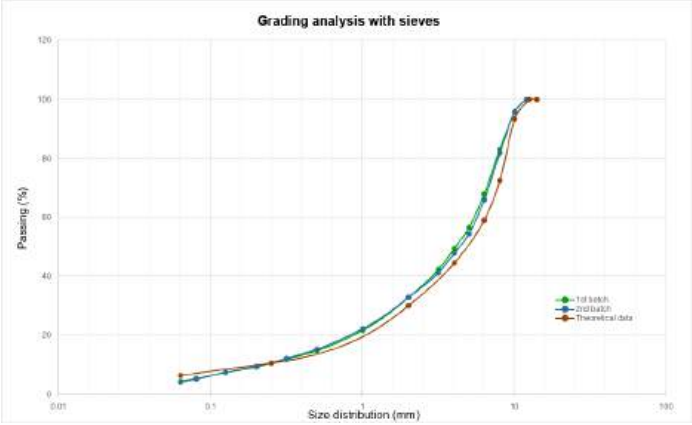

Figure 2.1: Grading analysis of BBE 0/10.

2.1.1.2. Bitumen emulsion

The cold asphalt is fabricated using bitumen emulsion, a mixture made of bitumen, water and emulsifier. For the crack propagation test, two different emulsions are used during the fabrication of the specimens. The first batch is made with an emulsion C72 and the second with an emulsion C65. 8.31% of emulsion is used in both cases in order to make the asphalt concrete. The bitumen emulsion was obtained in 2023 and has to be maintained at 40°C to avoid its degradation.

2.1.1.3. Other components

In the case of cold asphalt mix, extra water needs to be added to the mix. This amount is crucial because it affects the dry density of the asphalt. This behavior has been studied by Orosa et al. (Orosa et al., 2021). The goal is to achieve the highest possible density to minimize voids by using 2.6% of extra water according to the study.

2.1.2. Fabrication of specimens

2.1.2.1. Preparation of a manufacturing sheet

The manufacturing sheets, available in the Appendix, are established by indicating the necessary proportions of each fraction of the aggregates that ensure the desired recomposition of the grading curve. The total amount of asphalt pavement is set the value of each fraction is calculated according to the percentages of the table 1.1.

2.1.2.2. Mixing of materials

In the case of cold asphalt, there is no need of heating the mix, so to produce asphalt, first the aggregates are mixed and then, the water and the emulsion are added and mixed again. The result can be seen in the figure 2.2. This is an advantage in comparison to the hot asphalt because the aggregates has to be heated as well as the mould and a lot of energy has to be used.

Figure 2.2: Mixing of the components.

2.1.3. Compaction of the asphalt

The compaction of the ashpalt is made depending the type of test to conduct. In the case of complex modulus and crack propagation, the compaction is performed by using the machine PCG (Presse à Cisaillement Giratoire in French) according to the standard EN 12697-31. To prepare the specimens for testing, first the mix need to be compacted and then this compacted mixture is cut.
There are two different types of specimens made in the PCG machine: those for the complex modulus test and those for the cracking test. Technically, the machine is fabricated to make specimens of 150mm of height and diameter. However, the height of the specimen depends on the quantity of mass introduced in the mould.
For the crack propagation test, we need a height of 50mm. This machine allows us to adjust the number of turns it makes, thereby changing the height due to the percentage of voids. As the machine turns, it also ascends, producing a compressing. The mix is introduced into the cylindrical mould (figure 1.24) and compacted in the PCG machine to achieve the desired height.

This machine works by applying an axial force as it turns. The angle ϕ is equal to 0.82° and its

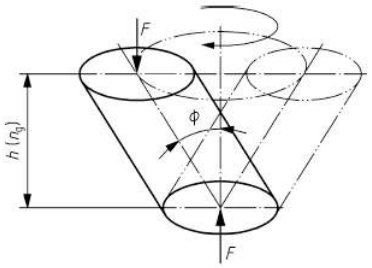

Figure 2.3: PCG characteristics.

rotational speed is 30 rpm. The combination of the force and the rotation results in a compaction effect comparable to that of a roller on a layer of asphalt.
During normal conditions, that means for heights of 150mm, the machine allows to calculate the compactness of the mix during compaction using the next equations:

$$\%voids = \frac{h_n - h_{min}}{h_n} \tag{1}$$

$$Compactness = 1 - \frac{\%voids}{100} \tag{2}$$

Where:

- h_{min}: minimal height of 150mm.
- h_n: height in the n gyrations.

Figure 2.4: PCG machine with mould containing asphalt mixture.

Figure 2.5: Compacting machine.

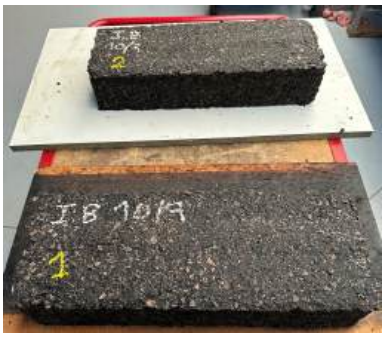

Figure 2.6: Compacted specimens.

The last type of specimen is the one for the rutting test. In this case, the rectangular parallelepiped specimen is made using a wheel compactor (see figure 2.5). The compacted specimens can be seen in the figure 2.6.

2.1.4. Curing of compacted specimens

After compacting, the specimens contain both air and water. Therefore, according to the standard NF EN 12697-54, they need to be maintained at 35°C for 21 days to achieve curing, lose the water, and acquire the desired properties. Also, the humidity of the environment has to be maintained at 20%. For that, the specimens are placed in a climatic chamber at the temperature and humidity required.

2.1.5. Sawing of specimens

In the case of complex modulus and crack propagation tests, once achieved the curing, the next step is to saw the specimens. There are two different types of sawing because each test requires a specific type of specimen.
According to the standard EN 12697-26 the specimen for the complex modulus test is prismatic (figure 2.7a) and its dimensions can be seen in the table 2.2. For the crack propagation test, according to the standard EN 12697-44, the specimen is semi-circular (figure 2.7b) and its dimensions can be seen in table 2.3. The sawing procedure is described in the figure 2.8.

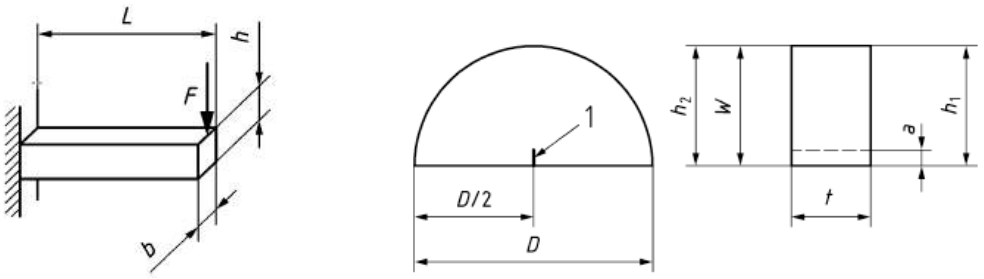

(a) Prismatic specimen.

(b) Semi-circular specimen.

Figure 2.7: Complex modulus and crack propagation specimens according to standards.

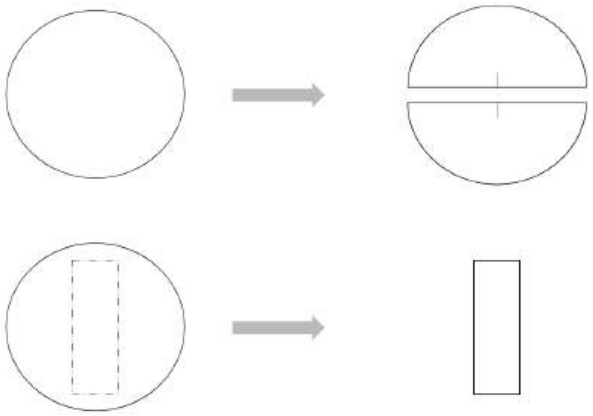

Figure 2.8: Description of both sawing types.

Prismatic specimens	
Dimension	**Value [mm]**
b	40
h	40
L	120

Table 2.2: Dimensions of complex modulus specimens.

Semi-circular specimens	
Dimension	**Value [mm]**
D	150
W	74
t	50
a	10

Table 2.3: Dimensions of crack propagation specimens.

(a) Equipment used for cutting the semi-circle and prismatic specimens.

(b) Equipment used for creating the cracks of the specimens.

Figure 2.9: Sawing of specimens.

2.1.6. Selection of specimens

2.1.6.1. Regarding to the SCB test

Once the semi-circular specimens were prepared, an experimental protocol for the cracking test was established. First, the void percentages of each specimen were calculated. For this, the

mass of each specimen is measured in a weighing machine in both air and water. The obtained void percentages were grouped by batch, that is, for each asphalt mix prepared at one time. The specimens were then divided between the two chosen test temperatures, 20°C and 5°C.
The distribution was not done arbitrarily. For each protocol, the mean void percentages and the standard deviations were calculated. The aim was to obtain an equal average void percentage for both protocols. In the end, a table with the results are presented in the appendix.

2.1.6.2. Regarding to the Complex Modulus test

In the case of the complex modulus specimens, after measuring all the dimensions, the void percentages are calculated following the same protocol as the SCB specimens and three specimens that meet the standards are selected from the six fabricated.

2.2. Complex modulus test

The stiffness test is essential for modeling the viscoelasticity of the material. E* represents the complex modulus (stiffness) of a viscoelastic material, such as asphalt, under cyclic loads. The tests are conducted according to the standard EN 12697-26+A1. There are different configurations, including 2, 3, and 4-points bending, as well as various specimen geometries such as prismatic, cylindrical, and tetrahedral. The chosen configuration is the 2-point bending test with prismatic specimens.

2.2.1. Preparation of specimens

The selection of the specimens is made according to their geometry as described in section 2.1.6. Following this selection, metal caps are glued to both ends of each specimen, with one cap allowing attachment to the machine and the other transmitting the load to the specimen. This operation is performed using special equipment designed to ensure the correct bonding of the pieces as well as the proper positioning of the specimen. This equipment can be seen in figure 2.10.

Figure 2.10: Equipment used for gluing the stiffness specimens.

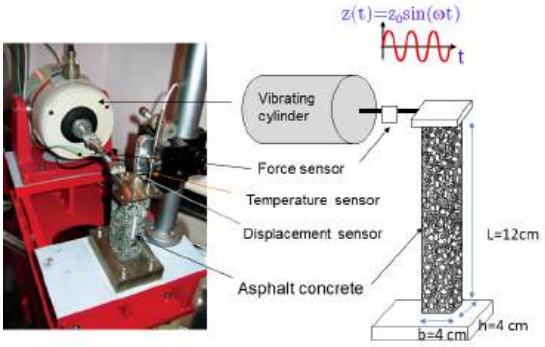

Figure 2.11: Complex modulus test.

2.2.2. Test device and parameters

The dimensions and the testing machine can be seen in the figure 2.11. This machine allows to make a two-point bending test at different temperatures and frequencies.

The specimen's base is fixed. The test involves applying a displacement ($z = z_0 * (sin\omega t)$) at a specific temperature and frequency to the top of the specimen and measuring the resulting force ($F = F_0 * (sin(\omega t + \delta))$. The deformation must not exceed $5 * 10^{-6} mm$ to remain within the linear viscoelastic domain.
Once the machine has computed the force, it also determines the complex modulus as follows:

$$E_1 = \gamma\left(\frac{F_0}{z_0}cos(\delta) + 10^{-6}\mu\omega^2\right) \tag{1}$$

$$E_2 = \gamma\left(\frac{F_0}{z_0}sin(\delta)\right) \tag{2}$$

Where:
E_1 : real modulus
E_2 : imaginary modulus
δ : phase angle
γ : shape factor, such as :

$$\gamma = \frac{4L^3}{bh^3} \tag{3}$$

μ : mass factor, such as :

$$\mu = \frac{M}{4} + m \tag{4}$$

$$|E^*| = \sqrt{E_1^2 + E_2^2} \tag{5}$$

$$\psi = arctan\left(\frac{E_2}{E_1}\right) \tag{6}$$

The device used for conducting the complex modulus tests is the SYMERIS machine (SYstème de MEsure de la RIgidité Standard in French), placed in a hermetically sealed climatic chamber. The tests were performed at temperatures ranging from -20°C to 50°C and at loading frequencies from 3 Hz to 40 Hz. The tested temperatures and frequencies are summarized in table 2.4. According to the standard, after changing the temperature of the climatic chamber, the specimen has to remain in the chamber for at least 4 hours in order to perform the test.

Temperatures [°C]	-20, -10, 0, 10, 20, 30, 40, 50
Frequencies [Hz]	3, 10, 25, 30, 40

Table 2.4: Testing temperatures and frequencies.

(a) Climatic chamber. (b) SYMERIS machine.

Figure 2.12: Devices used for the complex modulus test.

2.3. Crack propagation test

The goal of the semi-circular bending (SCB) test is to determine the tensile strength or fracture toughness of an asphalt mixture for the assessment of the potential for crack propagation.
This test is also called a 3-point bending test because the specimens are placed on two supports, with the load applied from the top, making this the third point.

2.3.1. Test parameters

The arrangement of the device can be seen in figure 2.13. The load is applied from the top using a mechanical power press at 5 mm/min. Regarding the temperature, the test is conducted at 20°C and 5°C. To achieve the desired temperatures, the specimens must remain in a climatic chamber for at least 4 hours. The center-to-center distance of the roller bearings is 120 mm.

2.3.2. Data acquisition and analysis of results

The EUROTEST-200 is the mechanical press used. It allows us to obtain the force-displacement curves during the test. Additionally, it enables the user to generate an Excel file with the data over time.

Figure 2.13: Arrangement of SCB specimens.

(a) Mechanic press.

(b) Climatic chamber.

Figure 2.14: Devices for the SCB test.

2.4. Rutting test

The rutting test is conducted using a mlpc ornieureur machine type (see figure 2.15) according to the NF EN 12697-22+A1 standard. This test is performed simultaneously on two specimens, following the procedure outlined below:

1. **Initial Measurements**: The height of each specimen is measured at 25 points (figure 2.16b);

2. **Initial Cycle Test**: A 1000-cycle test is conducted at room temperature, after which the heights are measured again;

3. **Heating and Final Test**: The specimens are maintained at 60°C for at least 12 hours in the machine. Following this, the heights are measured after 30, 100, 300, 1000, 3000, 10000 and 30000 cycles;

4. **Test Conclusion**: The test is concluded either when 30000 cycles are completed or when the average rut depth reaches 20 mm.

After concluding the test, the measured data is plotted for each specimen, displaying the percentage of depth versus the number of cycles. This type of graph allows to see the evolution of the rutting effect over the cycles at high temperature and to determinate the ability of the asphalt to resist rutting. The percentage of depth is calculated as follows:

$$P_i = 100 \sum_{j=1}^{15} \frac{d_{ij} - d0j}{15h} \tag{1}$$

Where:

- d_{ij}:is the localized distance between the reference surface and point j, in millimeters (mm), at measurement sequence i;
- d_{0j}:is the initial measurement of d_{ij} in millimeters (mm);
- h: is the thickness of the specimen, in millimeters (mm).

Figure 2.15: Rutting test machine.

Conclusions:
The entire process involved in the fabrication of the asphalt, along with its results, as well as the

(a) Specimen in rutting machine.

(b) Measurement of specimens height.

Figure 2.16: Rutting test execution.

machines and devices used, for the characterization were introduced. Additionally, the procedures to obtain these results were explained. In the next chapter, the results of these tests will be presented in the form of various graphs, and the goal will be to understand and explain these results.

Chapter 3

Experimental results

Introduction

In this chapter the results of the experimental tests presented in the second chapter will be showed. In the first part the results of the complex modulus test are shown as the isochrone, isotherm, Cole-Cole, Black and master curves. In the second part the results of the crack propagation test are shown as column graphs for the average values of maximal force, displacement at maximal force, rupture energy and the Cracking Resistance Index (CRI). Finally, the results of the rutting test are presented as depth average of rutting versus number of cycles.

3.1. Complex modulus results

The SYMERIS machine allows to obtain the complex modulus magnitud and the phase angle for different temperatures and frequencies. After obtaining the results, a Python code is used in order to obtain graphics results to simplify the visualization.

3.1.1. Isochrone and isotherm curves

The isotherm curves are shown in figures 3.1a and 3.2b. These curves illustrate the sensitivity of the viscoelastic properties of bituminous asphalt to loading frequency. The graphs demonstrate that the magnitude of the complex modulus tends to increase with increasing loading frequency, while the phase angle decreases. This effect is accentuated at high temperatures. At low temperatures, the material becomes elastic, which results in a phase angle tending towards zero.
The isochrone curves are shown in figures 3.2a and 3.1b. In this case, this curves represent the sensitivity of the viscoelastic properties to the temperature. As the temperature increases, the modulus decreases and the phase angle increases. This means that as the temperature increases the behavior becomes more viscous and as the temperature decreases the material becomes more elastic. At low temperatures (e.g -20°C) the phase angle is near to 0, this denotes that the imaginary part of the complex modulus is near 0.

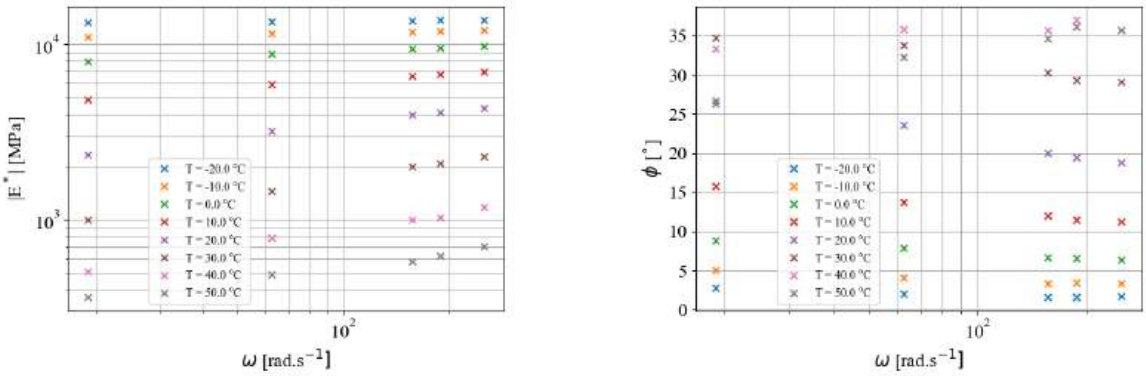

(a) Isothermal of the modulus magnitude.

(b) Isothermal of the phase angle.

Figure 3.1: Isothermal curves for the tested asphalt.

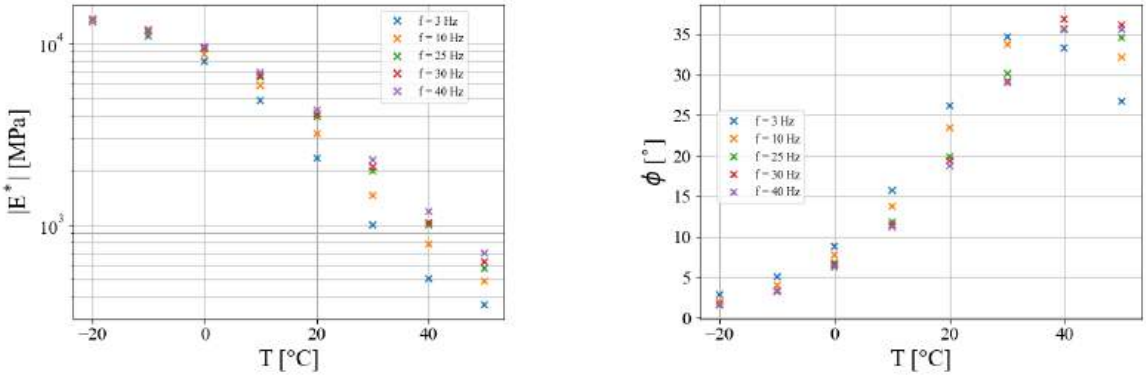

(a) Isochrone of the modulus magnitude.

(b) Isochrone of the phase angle.

Figure 3.2: Isochrone curves for the tested asphalt.

3.1.2. Cole-Cole and Black curves

The figures 3.3a and 3.3b represent the Black and Cole-Cole diagrams. The experimental points form unique curves in both diagrams, showing that the time-temperature superposition principle mentioned in section 1.3.1.1 is well applicable in the linear viscoelastic domain of the studied material.

3.1.3. Master curves

The master curves are essential diagrams that represent the behavior of asphalt over a wide range of frequencies for a specific temperature. To construct these diagrams, it is necessary to obtain the shift factors a_T. These factors are calculated using the Kramers-Kronig relationships (Booij and Thoone, 1982), as specified in section 1.3.1.1.3. To validate these coefficients, the relationship $\frac{dlog|E*|}{dlog\omega}$ as a function of $\delta\frac{\pi}{2}$ is plotted (see figure 3.4).

The figure shows that the Kramer-Kronig relation is validated. However, there are some points that

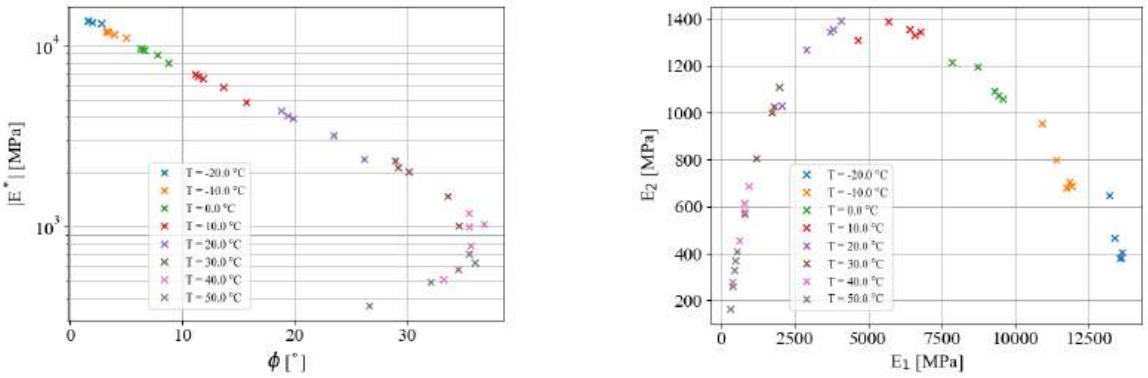

(a) Black curve.

(b) Cole-Cole curve.

Figure 3.3: Complex modulus in Cole-Cole and black diagrams.

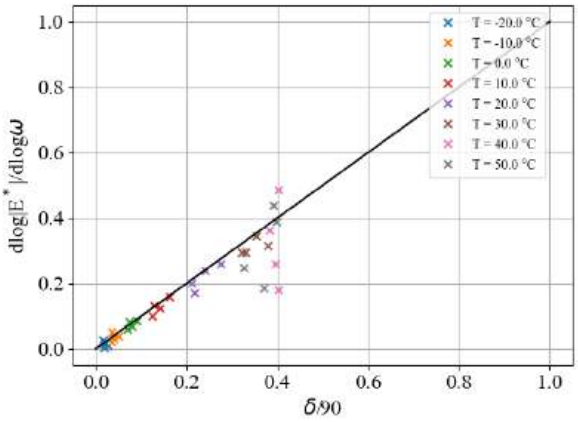

Figure 3.4: Validation of the Kramers-Kronig relation.

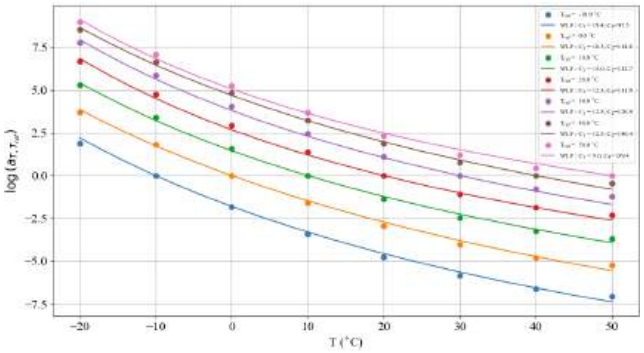

Figure 3.5: Shift factors of each temperature.

are distanced from the relationship, specially a high temperatures. This same observation is made in the works of Chailleux et al. (Chailleux et al., 2006) for high frequencies, and they concluded that this divergence is attributed either to a nonlinearity of the material under these solicitation conditions or to a lack of precision in the experimental measurements.
The master curve obtained by using the shift factors (figure 3.5) as well as the Huet-Sayegh and generalized Maxwell models are represented in the figure 3.6.
The parameters obtained of the Huet-Sayegh model this approximation are found in the table 3.1. Moreover, the parameters of the generalized Maxwell model are found in the appendix.

E_∞	E_0	δ	τ	k	h
187	15800	2.13	0.00512	0.17	0.58

Table 3.1: Huet-Sayegh model parameters.

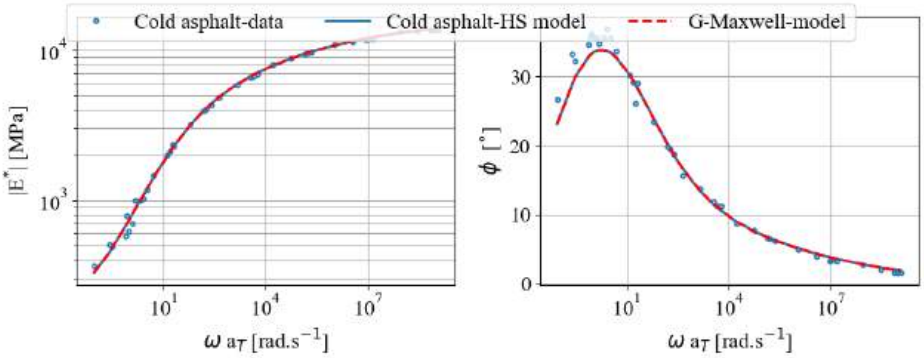

Figure 3.6: Master curve, Huet-Sayegh and generalized Maxwell models for the experimental data.

3.2. Crack propagation test results

The results as force-displacement curves are seen in the figure 3.7.

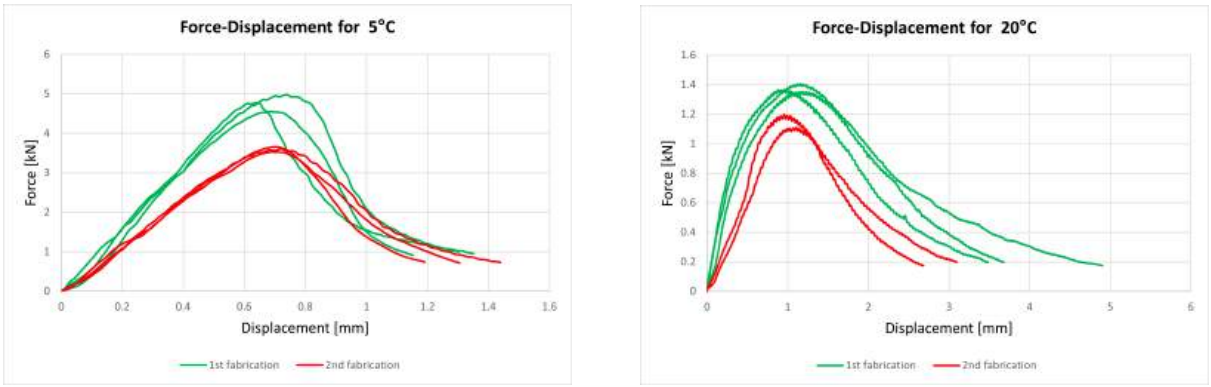

(a) Force-displacement curves for 5°C.

(b) Force-displacement curves for 20°C.

Figure 3.7: Results of SCB test.

3.2.1. Cracking properties

Different calculations are found in the bibliography in order to characterize the specimens behavior. The cracking properties analysed are the maximum force, the deformation at maximum force, the total fracture energy, and the Cracking Resistance Index (CRI).

- $\boldsymbol{F_{max}}$: The maximum force during testing is directly recorded from the experimental results.
- $\boldsymbol{\varepsilon_{max}}$: The deformation at maximum force is calculated from the displacement at maximum force. The expression is proposed in the standard NF EN 12697-44 for the cracking test on semi-circular specimens.

$$\boldsymbol{\varepsilon_{max} = \frac{u_{F_{max}}}{W} * 100} \quad (1)$$

where **W** is the average height of the specimen.

- G_f: The total fracture energy is calculated using the formula proposed in RILEM TC 50-FMC. (TCS, 1985)

$$G_f = \frac{\int f du}{B(W - a_0)} \tag{2}$$

where **B** is the average thickness of the specimen and a_0 is the notch depth.

- **CRI**: The Cracking Resistance Index (CRI) is a parameter defined by the ratio between the total fracture energy and the maximum force, expressed as:

$$CRI = \frac{G_f}{F_{max}} \tag{3}$$

where G_f is expressed in N/m and the maximum force in kN. This parameter is proposed by Kaseer et al. (Kaseer et al., 2018), who define this property as a parameter that allows quantifying the mechanical response of bituminous asphalt in terms of the energy required for cracking relative to the strength of these materials.

3.2.2. Effects of temperature on cracking properties

The fracture parameters enumerated in the previous paragraph are now represented as column graphics for the different test protocols, allowing the visualization of the effect of the temperature and the quantity of bitumen on the asphalt behavior regarding to cracking properties.

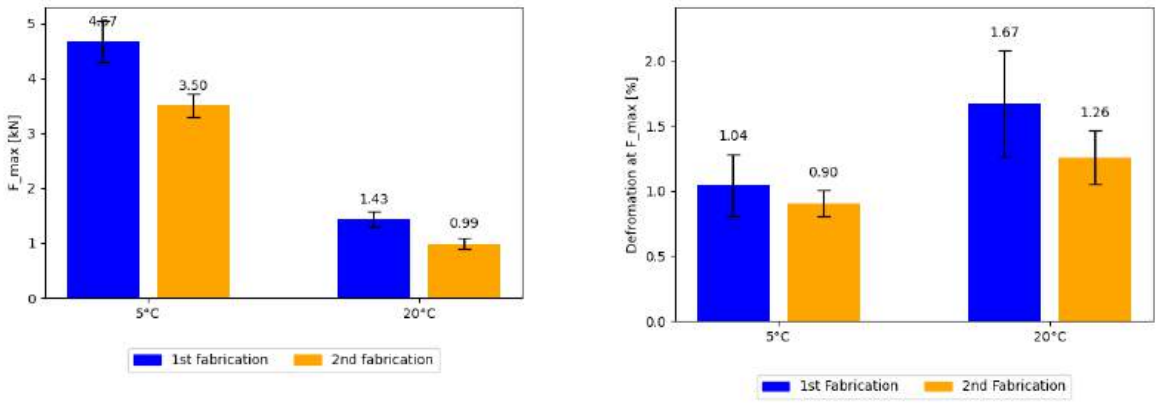

(a) Maximal force during testing.

(b) Deformation at maximal force.

Figure 3.8: Effect of temperature and bitumen quantity on maximal force and deformation at maximal force.

The figures 3.8a and 3.8b illustrate the sensibility of the maximal force and the deformation at maximal force to the temperature and the bitumen content. A significant impact of temperature on both the maximal force and the deformation at maximal force can be noted. As the temperature increases, the maximal force decreases, whereas the deformation at maximal force increases. Specifically, when the temperature rises from 5°C to 20°C, there is a 70% reduction in the maximal force and a 32% increase in deformation, for specimens from the same batch. This phenomenon is attributed to the ductility of the material. As the temperature increases, the material becomes more ductile, resulting

in a reduced force requirement to achieve the same level of deformation.
In terms of bitumen content, the first fabrication has a higher bitumen content, which results in an increase in both the maximal force and the deformation at maximal force. This could be attributed to the void percentages in the mix. The second batch has a higher content of voids, causing the fractures to propagate more easily through these voids.

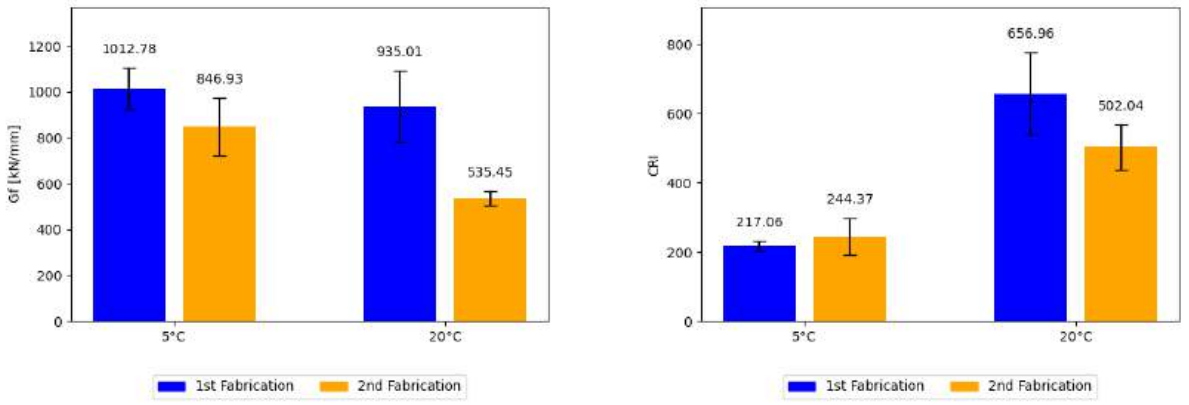

(a) Fracture energy.

(b) Cracking resistance index.

Figure 3.9: Effect of temperature and bitumen quantity on fracture energy and cracking resistance index.

Continuing with the sensitivity to temperature and bitumen content, figures 3.9a and 3.9b demonstrate their influence on fracture energy and the Cracking Resistance Index (CRI). For fracture energy, a relatively less significant variation is observed with changes in both temperature and bitumen content. The fracture energy decreases as the temperature increases, and an opposite effect is noted with increasing bitumen content. Specifically, when the temperature rises from 5°C to 20°C, the fracture energy decreases by 20%, and a 24% variation is seen when altering the bitumen content. This is because, as the maximal force decreases with increasing temperature, the area under the force-deformation curve diminishes. However, the concurrent increase in deformation compensates by enlarging the area under the curve, resulting in only modest changes in fracture energy.
The Cracking Resistance Index (CRI) exhibits a significant change with varying temperatures, while increasing the bitumen content does not lead to a noticeable change in the CRI. This behavior can be explained by the CRI's calculation as the fracture energy divided by the maximal force. Since the fracture energy does not vary substantially with temperature, a lower temperature results in a higher maximal force, leading to a lower CRI, and vice versa.

3.3. Rutting test results

The last test had the goal to analyse the rutting effect. This test was conducted at 60°C following the standard NF EN 12697-22+A1 and the results can be seen in the figure 3.10. It can be noticed that the graph contents two different zones, first a decelerating rutting from 0 to 3000 cycles and then a stationary zone where the rutting increment is made with a constant rate from 3000 to 30000 cycles. The specimens after testing can be seen in the figure 3.11.

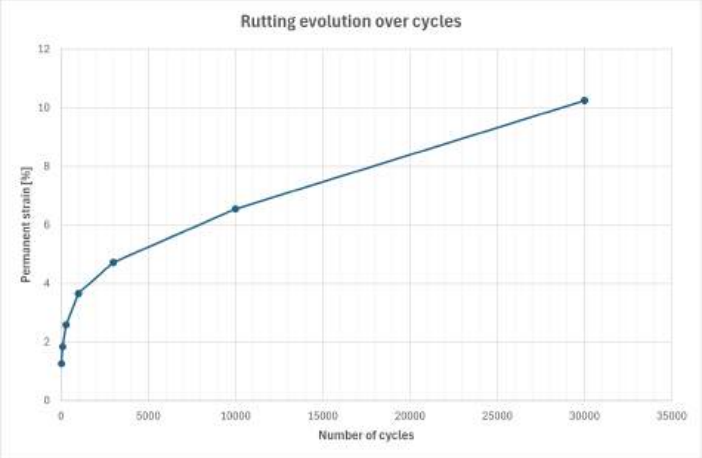

Figure 3.10: Rutting effect versus number of cycles at 60°C.

Figure 3.11: Rutting specimens after testing.

Conclusions:

In this chapter, the results of the complex modulus, the crack propagation and rutting tests have been presented. Regarding to the complex modulus, the results showed a decreasing of the modulus and an increasing of the phase angle when rising the temperature. The same conclusion is seen in different articles as Dong et al. (2024) and Quezada and Chazallon (2020). Also a model representing the behavior for a long range of frequency loads was obtained by using these test results. Regarding to the crack propagation tests, the results showed that when decreasing the temperature and increasing the bitumen quantity, the strength of the material increased by showing an incremented maximal force. However, more temperatures and bitumen contents should be tested in order to correctly characterize these behaviors. The last property tested was the rutting resistance. The results showed that as the cycles of loads were incremented, the rutting was increased but at different rates. This conclusion is seen in different authors as Zhang et al. (2020b) and Lu et al. (2018). The next chapter presents the general conclusion of this study and proposals for improvement.

Chapter 4

Numerical study of cracking cold asphalt

Introduction

The goal of this chapter is to model the viscoelastic behavior along with the crack propagation of the bituminous mixture. For that, first a behavior law obtained by a generalized Maxwell model is discretised. Next, the theory behind the phase-field method is introduced and the week formulations are presented, incorporating internal research conducted by Cerema. Finally, the SCB test is simulated by varying different parameters introduced in the second part.

4.1. Discretization of the behavior laws

When studying the behavior of the bituminous mixtures, a large number of rheological models are found in the bibliography as shown in section (1.3.2). In this study, the rheological model chosen for representing the behavior of the cold asphalt mixtures is the Generalized Maxwell model.
Where $\mathbb{C}_i^e$ and $\mathbb{C}_i^v$ represent the elastic and viscous tensors of the i branch. Furthermore, τ_i is called

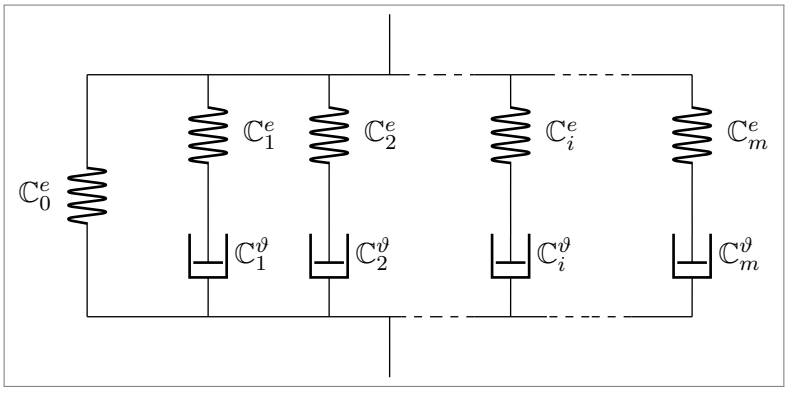

Figure 4.1: Generalized Maxwell model (GM)

relaxation time where $\tau_i * \mathbb{C}_i^e = \mathbb{C}_i^v$.
The equivalent stress of the model is defined as:

$$\boldsymbol{\sigma}(t) = \boldsymbol{\sigma}_0(t) + \sum_{i=1}^{m} \boldsymbol{\sigma}_i(t) \tag{1}$$

With:

$$\boldsymbol{\sigma}_0(t) = \mathbb{C}_0^e : \boldsymbol{\varepsilon}(t) \qquad \boldsymbol{\sigma}_i(t) = \mathbb{C}_i^e : (\boldsymbol{\varepsilon} - \boldsymbol{\varepsilon}_i^v) = \mathbb{C}_i^v : \dot{\boldsymbol{\varepsilon}}_i^v \tag{2}$$

And:

$$\dot{\boldsymbol{\sigma}}_i(t) = \mathbb{C}_i^e : (\dot{\boldsymbol{\varepsilon}} - \dot{\boldsymbol{\varepsilon}}_i^v) \tag{3}$$

Using the equations (2) and (4) we can find the differential equation that relates the stress in one branch and the total deformation:

$$\dot{\boldsymbol{\sigma}}_i(t) + \frac{1}{\tau_i}\boldsymbol{\sigma}_i(t) = \mathbb{C}_i^e \cdot \dot{\boldsymbol{\varepsilon}}_i \tag{4}$$

Which solutions is:

$$\boldsymbol{\sigma}_i(t) = \int_{t_0}^{t} \mathbb{C}_i^e e^{-\frac{(t-t')}{\tau_i}} : d\boldsymbol{\varepsilon}(t') \tag{5}$$

Introducing the equations (2) and (5) in (1):

$$\boldsymbol{\sigma}(t) = \int_{t_0}^{t} \mathbb{C}_0^e + \sum_{i=1}^{m} \mathbb{C}_i^e e^{-\frac{(t-t')}{\tau_i}} : d\boldsymbol{\varepsilon}(t') \tag{6}$$

Solving equations of this type often involves lengthy simulations. To mitigate this, an exponential algorithm proposed by Bazant and Smilauer (Majorana, 1989) is employed. Thus, time is discretised into sub-intervals $\Delta_n t$ such as $t_{n+1} = t_n + \Delta_n t$. The equation (5) results:

$$\boldsymbol{\sigma}(t_{n+1}) = \int_{t_0}^{t_{n+1}} \mathbb{C}_i^e e^{-\frac{(t_{n+1}-t')}{\tau_i}} : d\boldsymbol{\varepsilon}(t') \tag{7}$$

Also the time can be divided into two intervals as $t_0 < t < t_n$ and $tn < t < t_{n+1}$, knowing the result of the first interval. Hence:

$$\boldsymbol{\sigma}_i(t_{n+1}) = e^{-\frac{(\Delta_n t)}{\tau_i}}\boldsymbol{\sigma}_i(t_n) + \int_{t_n}^{t_{n+1}} \mathbb{C}_i^e e^{-\frac{(t_n+\Delta_n t-t')}{\tau_i}} : d\boldsymbol{\varepsilon}(t') \tag{8}$$

To calculate the unknown integral, the following approximation can be used:

$$\frac{d\boldsymbol{\varepsilon}(t')}{dt'} = \frac{\boldsymbol{\varepsilon}(t_{n+1}) - \boldsymbol{\varepsilon}(t_n)}{\Delta_n t} \tag{9}$$

Thus the equation (8) results:

$$\boldsymbol{\sigma}_i(t_{n+1}) = e^{-\frac{(\Delta_n t)}{\tau_i}}\boldsymbol{\sigma}_i(t_n) + \frac{\tau_i}{\Delta_n t}(1 - e^{-\frac{(\Delta_n t)}{\tau_i}})\mathbb{C}_i^e : \Delta_n\boldsymbol{\varepsilon} \tag{10}$$

Finally, by substituting equation (10) into (1):

$$\Delta_n\boldsymbol{\sigma} = \mathbb{C}(\Delta_n t) : \Delta_n\boldsymbol{\varepsilon} + \widetilde{\boldsymbol{\sigma}}(t_n) \tag{11}$$

With:

$$\mathbb{C}(\Delta_n t) = \mathbb{C}_0 + \sum_{i=1}^{m} \frac{\tau_i}{\Delta_n t}(1 - e^{-\frac{(\Delta_n t)}{\tau_i}})\mathbb{C}_i \tag{12}$$

$$\widetilde{\boldsymbol{\sigma}}(t_n) = \sum_{i=1}^{m}(e^{-\frac{(\Delta_n t)}{\tau_i}} - 1)\boldsymbol{\sigma}_i(t_n) \tag{13}$$

Considering linear isotropic viscoelastic behavior, the fourth-order tensor $\mathbb{C}$ can be defined by two scalar viscoelastic kernels, λ and μ (Salencon, 2016).

$$\Delta_n \boldsymbol{\sigma} = \lambda(\Delta_n t) trace(\Delta_n \boldsymbol{\varepsilon})\boldsymbol{I} + 2\mu(\Delta_n t)\Delta_n \boldsymbol{\varepsilon} + \widetilde{\boldsymbol{\sigma}}(t_n) \tag{14}$$

Where:

$$\lambda(\Delta_n t) = \lambda_0 + \sum_{i=1}^{m} \frac{\tau_i}{\Delta_n t}\left(1 - \exp\left(-\frac{\Delta_n t}{\tau_i}\right)\right)\lambda_i \tag{15a}$$

$$\mu(\Delta_n t) = \mu_0 + \sum_{i=1}^{m} \frac{\tau_i}{\Delta_n t}\left(1 - \exp\left(-\frac{\Delta_n t}{\tau_i}\right)\right)\mu_i \tag{15b}$$

4.2. Phase-field method theory

Following with intern work made in Cerema, (Kouevidjin et al., 2024), in current development, taking into account the damage of the material, the equations of the mechanical problem become:

$$\begin{cases} div(\boldsymbol{\sigma}(\underline{x}, t)) = 0 & \text{in } \Omega \\ \boldsymbol{\sigma} = g(d)\left(\mathbb{C}_0 : \varepsilon + \sum_{i=1}^{m} \mathbb{C}_i : (\boldsymbol{\varepsilon} - \boldsymbol{\varepsilon}_i^v)\right) & \text{sur } \Omega \\ \boldsymbol{\sigma}.\underline{n} = \underline{T}^d & \text{on } \Gamma \end{cases} \tag{1}$$

And also:

$$\begin{cases} \dot{d} = \frac{1}{\xi}\left(\frac{2\ell}{c_\omega} div\big(G_c(d,\zeta)\underline{grad\, d}\big) - g'(d)\mathcal{H} - \frac{\partial G_c}{\partial d}(d,\zeta)\gamma\ell - \frac{G_c(d,\zeta)}{\ell c_\omega}\omega'(d)\right) & \text{in } \Omega \\ \underline{grad\, d}.\underline{n} = 0 & \text{on } \Gamma \end{cases} \tag{2}$$

Where $\dot{d}$ is the damage velocity and $g(d)$ a damage energy function that translates the loss of stiffness associated with the evolution of the damage. This function verifies the following conditions:

- $g(0) = 1$ and $g(1) = 0$;
- $g'(d) \leq 0$ and $g'(1) = 0$.

In addition, $\omega(d)$ is the geometric crack function defined as:

- $\omega(d) = 1 \in [0, 1]$;

- $\omega(0) = 0$ and $\omega(1) = 1$.

The selected expression of $\omega(d)$ is the following quadratic form:

$$\omega(d) = d^2 \tag{3}$$

Furthermore, c_ω is a normalization parameter defined as:

$$c_\omega = 4 \int_0^1 \sqrt{\omega(z)} dz = 2 \tag{4}$$

Finally, G_c and $\gamma\ell$ are defined as:

$$\begin{cases} G_c(d,\zeta) = G_{c0}(1 + g(d)\alpha\zeta)^\beta \quad \text{with} \quad \zeta = \int_0^t \sqrt{\sum_{i=1}^m (\dot{\varepsilon_i^v} : \dot{\varepsilon_i^v})} \\ \gamma\ell = \frac{1}{\ell c_\omega}(\omega(d) + \ell^2 |\underline{grad}\, d|^2 \end{cases} \tag{5}$$

G_c allows to couple damage and viscosity by taking into account the function g(d) and the effective viscous strain ζ.

4.3. Week formulation

4.3.1. Mechanical problem

Let's consider the border $\partial\Omega$ subdivided into two parts Γ_u on which the Dirichlet conditions are imposed ($\underline{u} = \underline{U}^d$) and Γ_T on which the force conditions are imposed ($\boldsymbol{\sigma}.\underline{n} = \underline{T}^d$). One defines the kinematically admissible $\mathcal{V}_u$ and kinematically admissible at zero $\mathcal{V}_u^0$ spaces:

$$\mathcal{V}_u = \left\{ \underline{\hat{u}} \in \mathcal{H}^1(\Omega) : \underline{\hat{u}} = \underline{U}^d \text{ on } \Gamma_u \right\} \quad \text{and}$$
$$\mathcal{V}_u^0 = \left\{ \underline{\hat{u}} \in \mathcal{H}^1(\Omega) : \underline{\hat{u}} = \underline{0} \text{ on } \Gamma_u \right\}$$

The week formulation of the mechanical problem (1) can be obtained by multiplying the divergence equation by a virtual displacement field called δu and by integrating on the domain Ω.

$$\int_\Omega div(\boldsymbol{\sigma}) \delta\underline{u} d\Omega = 0 \tag{1}$$

By applying the properties of the divergence, the equation (1) becomes:

$$\int_{\partial\Omega} (\boldsymbol{\sigma}.\underline{n}) \delta\underline{u} ds - \int_\Omega \boldsymbol{\sigma} : \delta\underline{u} d\Omega = 0 \tag{2}$$

$$\int_\Omega \boldsymbol{\sigma} : \boldsymbol{\varepsilon}(\underline{u}) d\Omega = \int_{\Gamma_T} \underline{T}^d . \underline{u} d\Gamma \tag{3}$$

Being $\underline{u}^{n+1,(k)}$ the unknown displacement field at time t_{n+1} and at iteration k and by $d^{n+1,(k-1)}$ the fixed damage field at time t_{n+1} and at iteration k-1, the week formulation becomes by using the

equations (3) and (14):
Find $\underline{u}^{n+1,(k)} \in \mathcal{V}_u$, such as:

$$\left\{\begin{array}{l} \displaystyle\int_\Omega \left(\left(1-d^{n+1,(k-1)}\right)^2+k_r\right)\left(\lambda(\Delta_n t)\mathrm{tr}\left(\boldsymbol{\varepsilon}^{n+1,(k)}\right)\mathbb{I}+2\mu(\Delta_n t)\boldsymbol{\varepsilon}^{n+1,(k)}\right)\cdot\boldsymbol{\varepsilon}(\underline{\hat{u}})\,\mathrm{d}\Omega = \\ \displaystyle\int_\Omega \left(\left(1-d^{n+1,(k-1)}\right)^2+k_r\right)\left(\lambda(\Delta_n t)\mathrm{tr}(\boldsymbol{\varepsilon}^{n})\mathbb{I}+2\mu(\Delta_n t)\boldsymbol{\varepsilon}^{n}-\boldsymbol{\sigma}^n-\widetilde{\boldsymbol{\sigma}}^n\right)\cdot\boldsymbol{\varepsilon}(\underline{\hat{u}})\,\mathrm{d}\Omega+ \\ \displaystyle\int_{\Gamma_T}\underline{T}^{d\,n+1}\cdot\underline{\hat{u}}\,\mathrm{d}\Gamma_T \quad \forall\,\underline{\hat{u}}\in\mathcal{V}_u^0 \end{array}\right. \tag{4}$$

4.3.2. Phase field problem

Let $\mathcal{V}_d^0$ be the admissible damage field space at zero defined by:

$$\mathcal{V}_d^0 = \left\{\hat{d} \in \mathcal{H}^1(\Omega) \,:\, \hat{d}=0 \text{ on } \partial\Omega\right\}$$

Multiplying the equation (2) by a test function $\hat{d}$ and integrating over Ω, one gets:

$$\int_\Omega\left[\left(\frac{2\ell}{c_\omega}G_c(d,\zeta)\underline{grad}\,d\cdot\underline{grad}\,\hat{d}\right)+\left(\xi\dot{d}+g'(d)\mathcal{H}+\frac{\partial G_c}{\partial d}(d,\zeta)\gamma_\ell+\frac{1}{\ell c_\omega}G_c(d,\zeta)\omega'(d)\right)\hat{d}\right]\mathrm{d}\Omega=0 \tag{5}$$
$$\forall\,\hat{d}\in\mathcal{V}_d^0$$

Introducing the temporal discretization, the weak form of the phase field evolution problem at time t_{n+1} and at iteration k for a fixed displacement field $\underline{u}^{n+1,(k)}$ is formulated as follows:
Find $d \in \mathcal{V}_d^0$, such as:

$$\begin{array}{l}\displaystyle\int_\Omega\left[\left(\frac{2\ell}{c_\omega}G_c\left(d^{n+1,(k)},\zeta^{n+1,(k)}\right)\underline{grad}\,d^{n+1,(k)}\cdot\underline{grad}\,\hat{d}\right)+\left(\xi\dot{d}^{n+1,(k)}+g'\left(d^{n+1,(k)}\right)\mathcal{H}^{n+1,(k)}+\right.\right. \\ \left.\left.\dfrac{\partial G_c}{\partial d}\left(d^{n+1,(k)},\zeta^{n+1,(k)}\right)\gamma_\ell+\dfrac{1}{\ell c_\omega}G_c\left(d^{n+1,(k)},\zeta^{n+1,(k)}\right)\omega'\left(d^{n+1,(k)}\right)\right)\hat{d}\right]\mathrm{d}\Omega=0 \quad \forall\hat{d}\in\mathcal{V}_d^0\end{array} \tag{6}$$

with:

$$\dot{d}^{n+1,(k)} \simeq \frac{d^{n+1,(k)}-d^n}{\Delta_n t} \tag{7a}$$

$$\mathcal{H}^{n+1,(k)} = \max\left(\overline{\Psi}_e^+\left(\boldsymbol{\varepsilon}^{n+1,(k)},\{\boldsymbol{\varepsilon}_i^{v,\,n+1,(k)}\}_{i=1}^{i=m}\right),\mathcal{H}^n\right) \tag{7b}$$

$$G_c\left(d^{n+1,(k)},\zeta^{n+1,(k)}\right) = G_{c0}\left[1+\alpha g(d^{n+1,(k)})\left(\zeta^n+\sqrt{\left(\sum_{i=1}^m \Delta_n\boldsymbol{\varepsilon}_i^{v+}:\Delta_n\boldsymbol{\varepsilon}_i^{v+}\right)}\right)\right]^\beta \tag{7c}$$

4.3.3. Finite element implementation in software GetFEM

The implementation of the problem is made in the library GetFEM (Renard and Poulios, 2021) by using a Python script.

4.3.4. Results and parameters influence

Different simulations have been made in order to model the experimental results. For that, different parameters as α, β (equation (5)) and the critical energy of the material can be varied. The results are seen in the figure 4.2.

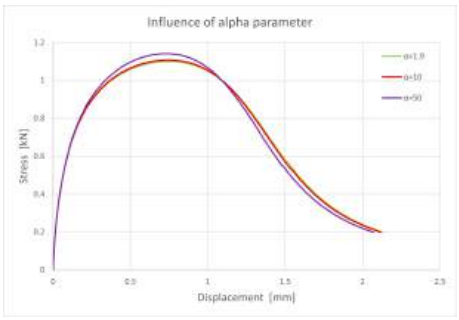

(a) Influence of alpha.

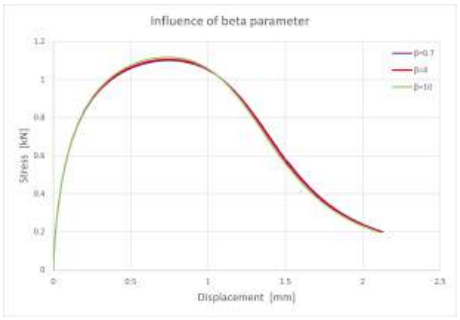

(b) Influence of beta.

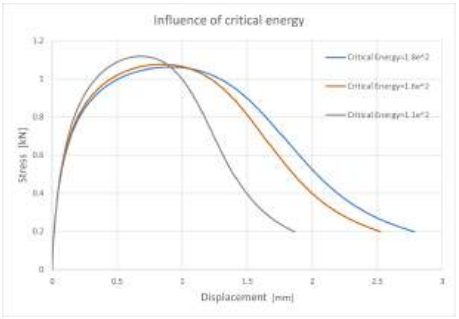

(c) Influence of critical energy.

Figure 4.2: Influence of different parameters on force-displacement curves.

4.3.5. Comparison between numerical and experimental

The final part of this work has for goal to obtain numerically the same results as the experimental chapter. The figure 4.3 denotes this comparison but a significant difference between both slopes is noticed. Even when varying different parameters, the difference persisted.

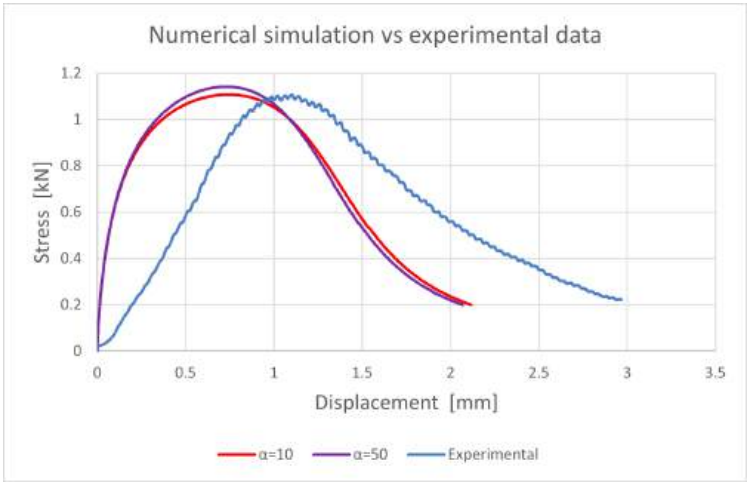

Figure 4.3: Numerical vs experimental curves of force-displacement.

Conclusions:

In this chapter the modeling of crack propagation in a viscoelastic material was developed. The viscoelastic behavior law and its discretization were first presented. Then, the theory of the phase

field method was developed and the test under bending load was simulated. A parametric study was conducted, demonstrating the dependence of the model on different parameters. However, the results were not similar to the experimental results and this could be cause by imperfections when conducting the experimental tests of the specimens in the mechanic press.

Conclusions

Cold asphalt emerges as a promising option for decarbonization efforts in the coming decades. However, the quality of this type of bituminous mixture is not really well known. In this context, this project was proposed with the objective of investigating the mechanical properties of the cold asphalt denominated BBE 0/10. This work involved two aspects, an experimental and a numerical component.

The experimental phase focused on three primary tests: the complex modulus that provided information about the viscoelastic properties and allowed to obtain the master curves of the asphalt concrete, the Semi-Circular Bend test (SCB) which gave information about the cracking resistance of the material at 5°C and at 20°C for two different contents of bitumen and finally, the rutting test that evaluated the permanent strain produced by vehicular loads. For each of these tests, asphalt samples were fabricated in different geometries and sizes according to the European standars.

As mentioned in the abstract, the properties of cold asphalt are generally less consistent compared to hot asphalt mixes. When comparing the results, the complex modulus test revealed that the modulus of cold asphalt is significantly lower than that of hot asphalt mixtures, indicating that the studied material exhibits greater deformability. At certain temperatures, the modulus was even reduced to half of that observed in a typical Hot Asphalt Mix BBSG 0/10. Regarding the rutting test, European standards do not provide specific guidelines for cold asphalt, as it is assumed that the material is not likely to experience significant permanent deformation. However, the results demonstrated that the rutting caused by the wheel exceeded the maximum limit allowed for hot asphalt mixtures. The numerical phase aimed to model the experimental results obtained by the Semi-Circular Bend test. For that, the viscoelastic behavior of the bituminous pavement was modeled and discretized based on the generalized Maxwell model obtained by the implementation of a Python code and a crack propagation model was introduced. Then, a finite element code using GetFEM was employed. The geometry, finite element parameters, and boundary conditions were coded to simulate the damage propagation problem. However, despite performing a parametric analysis, the simulation results did not align with the experimental data. This could be caused by the effect of imperfections when conducting the experimental test or to the measurement errors of the machine. The contact between the press and the specimens is not precisely parallel causing probably a variation in the slope of the graphics force-displacement. Also, a significant variation in results from the same batch was observed, which could also be attributed to the differences between each specimen.

Prospects

Based on the results obtained during this study, improvements can be considered. Firstly, in terms of the fabrication of SCB specimens, the PCG machine is currently designed for specimens with a height of 150 mm, which complicates the calculation of void percentages during compaction. Identifying a method to measure these voids would enable the production of more homogeneous batches, potentially reducing variation in the results. Regarding the mechanical properties, more temperatures on crack propagation conditions could be tested. Also, a device to improve the placing of the specimen could be developed to ameliorate the force-displacement results. Finally, future studies could be conducted to expand the knowledge of the mechanical properties of cold asphalt. The mixed mode for the SCB test and specially the aging of these bituminous mixtures. As the properties change over time, it is important to determinate if this variations could caused a premature damage in cold asphalt mixtures.

Bibliography

Al-Atroush, M. (2022). Structural behavior of the geothermo-electrical asphalt pavement: A critical review concerning climate change. *Heliyon*, 8(12):e12107.

Al-Mohammedawi, A. and Mollenhauer, K. (2024). Experimental investigation on fatigue and fracture behaviour of cold recycling materials. *Transportation Engineering*, 17:100258.

Aliha, M., Fazaeli, H., Aghajani, S., and Moghadas Nejad, F. (2015). Effect of temperature and air void on mixed mode fracture toughness of modified asphalt mixtures. *Construction and Building Materials*, 95:545–555.

Booij, H. C. and Thoone, G. P. J. M. (1982). Generalization of Kramers-Kronig transforms and some approximations of relations between viscoelastic quantities. *Rheologica Acta*, 21(1):15–24.

Chailleux, E., Ramond, G., Such, C., and De La Roche, C. (2006). A mathematical-based master-curve construction method applied to complex modulus of bituminous materials. *Road Materials and Pavement Design*, 7(sup1):75–92.

Chong, K. P. and Kuruppu, M. D. (1984). New specimen for fracture toughness determination for rock and other materials. *International Journal of Fracture*, 26:R59–R62.

Di Benedetto, H. and Corté, J. (2004). *Matériaux routiers bitumineux: Tome 2, Constitution et propriétés thermomécaniques des mélanges*. Number vol. 2 in Matériaux routiers bitumeux. Hermes Science Publications.

Dong, W., Ma, F., Fu, Z., Qin, W., Qi, C., He, J., and Li, C. (2024). Construction and examination of temperature master curve for asphalt with different aging extents. *Fuel*, 370:131819.

Gao, H., Yang, X., and Zhang, C. (2015). Experimental and numerical analysis of three-point bending fracture of pre-notched asphalt mixture beam. *Construction and Building Materials*, 90:1–10.

Griffith, A. A. (1920). The phenomena of rupture and flow in solids. *Philosophical Transactions of the Royal Society A*, 221:163–198.

Imaninasab, R., Loria-Salazar, L., and Carter, A. (2022). Integrated performance evaluation of asphalt mixtures with very high reclaimed asphalt pavement (rap) content. *Construction and Building Materials*, 347:128607.

Janssen, M., Zuidema, J., and Wanhill, R. (2004). *Fracture Mechanics: Fundamentals and Applications*.

Kaseer, F., Yin, F., Arámbula-Mercado, E., Epps Martin, A., Daniel, J. S., and Salari, S. (2018). Development of an index to evaluate the cracking potential of asphalt mixtures using the semi-circular bending test. *Construction and Building Materials*, 167:286–298.

Kim, K. W. and El Hussein, M. (1997). Variation of fracture toughness of asphalt concrete under low temperatures. *Construction and Building Materials*, 11(7-8):403–411.

Kim, Y. and Wen, H. (2002). Fracture energy from indirect tension testing. *Journal of the Association of Asphalt Paving Technologists*, 71:779–793.

Kouevidjin, A. B., Somé, S. C., Akkouche, H., Barthélémy, J.-F., Dhia, H. B., and Mouillet, V. (2024). Comparative analysis of phase field model for crack propagation in asphalt mixtures: Experimental and numerical investigation.

Krans, R. L., Tolman, F., and van de Ven, M. (1996). Semi-circular bending test: a practical crack growth test using asphalt concrete cores. In *Reflective Cracking in Pavements*.

Li, X.-J. and Marasteanu, M. O. (2010). Using Semi Circular Bending Test to Evaluate Low Temperature Fracture Resistance for Asphalt Concrete. *Experimental Mechanics*, 50(7):867–876.

Lu, Z., Fang, R., Yao, H., Hu, Z., and Liu, J. (2018). Evaluation and analysis of the traffic load–induced settlement of roads on soft subsoils with low embankments. *International Journal of Geomechanics*, 18.

Majorana, C. E. (1989). Mathematical modeling of creep and shrinkage of concrete, edited by z. p. bazant, 1988. wiley, isbn 0 471920576. price £65.00. *Communications in Applied Numerical Methods*, 5(6):423–423.

Olard, F. and Benedetto, H. D. (2003). General "2s2p1d" model and relation between the linear viscoelastic behaviours of bituminous binders and mixes. *Road Materials and Pavement Design*, 4(2):185–224.

Orosa, P., Pasandín, A., and Pérez, I. (2021). Compaction and volumetric analysis of cold in-place recycled asphalt mixtures prepared using gyratory, static, and impact procedures. *Construction and Building Materials*, 296:123620.

Pan, Y., Guo, H., Guan, W., and Zhao, Y. (2023). A laboratory evaluation of factors affecting rutting resistance of asphalt mixtures using wheel tracking test. *Case Studies in Construction Materials*, 18:e02148.

Quezada, J. C. and Chazallon, C. (2020). Complex modulus modeling of asphalt concrete mixes using the Non-Smooth Contact Dynamics method. *Computers and Geotechnics*, 117:103255.

Renard, Y. and Poulios, K. (2021). GetFEM: Automated FE Modeling of Multiphysics Problems Based on a Generic Weak Form Language. *ACM Transactions on Mathematical Software*, 47(1):1–31.

Riccardi, C., Cannone Falchetto, A., Wang, D., and Wistuba, M. (2017). Effect of cooling medium on low-temperature properties of asphalt binder. *Road Materials and Pavement Design*, pages 1–22.

Salencon, J. (2016). *Viscoélasticité pour le calcul des structures*.

Sayegh, G. (1966). *Contribution à l'étude des propriétés viscoélastiques des bitumes purs et des bétons bitumineux*. PhD thesis.

TCS, R. (1985). Draft recommendation: "determination of the fracture energy of mortar and concrete by means of three-point bend tests on notched beams". *Materials and Structures*, 18:484.

Wagoner, M. P., Buttlar, W. G., Paulino, G. H., and Blankenship, P. (2005). Investigation of the Fracture Resistance of Hot-Mix Asphalt Concrete Using a Disk-Shaped Compact Tension Test. *Transportation Research Record: Journal of the Transportation Research Board*, 1929(1):183–192.

Witczak, M., Kaloush, K., Pellinen, T., El-Basyouny, M., and Von Quintus, H. (2002). Simple performance test for superpave mix design: Nchrp report no. 465. washington dc: Transportation research board, national research council.

Xu, S., Ruan, P., Lu, Z., Liang, L., Han, B., and Hong, B. (2021). Effects of the high temperature and heavy load on the rutting resistance of cold-mix emulsified asphalt mixture. *Construction and Building Materials*, 298:123831.

Zhang, J., Zheng, M., Pei, J., Zhang, J., and Li, R. (2020a). Research on Low Temperature Performance of Emulsified Asphalt Cold Recycled Mixture and Improvement Measures Based on Fracture Energy. *Materials*, 13(14):3176.

Zhang, Y., Luo, X., Deng, Y., Hou, S., Shi, X., and Lytton, R. L. (2020b). Evaluation of rutting potential of flexible pavement structures using energy-based pseudo variables. *Construction and Building Materials*, 247:118391.

Appendix

Formule	Sieve	20	16	14	12.5	10	8	6.3	4	2	0.25	0.063
	Int	#NOM?	#NOM?	#NOM?	#NOM?	#NOM?	#NOM?	#NOM?	#NOM?	#NOM?	#NOM?	#NOM?
	1st gran	100	100	100	100	95.6784	83.1647	68.0038	56.6358	32.9127	9.39053	4.43794

Base granulometry	100	99.8	98.3	98	94	72	60	42	32	12	6.4
Variation	0	-0.2	-1.7	-2	-1.67838	-11.1647	-8.00381	-14.6358	-0.91269	2.60947	1.96206

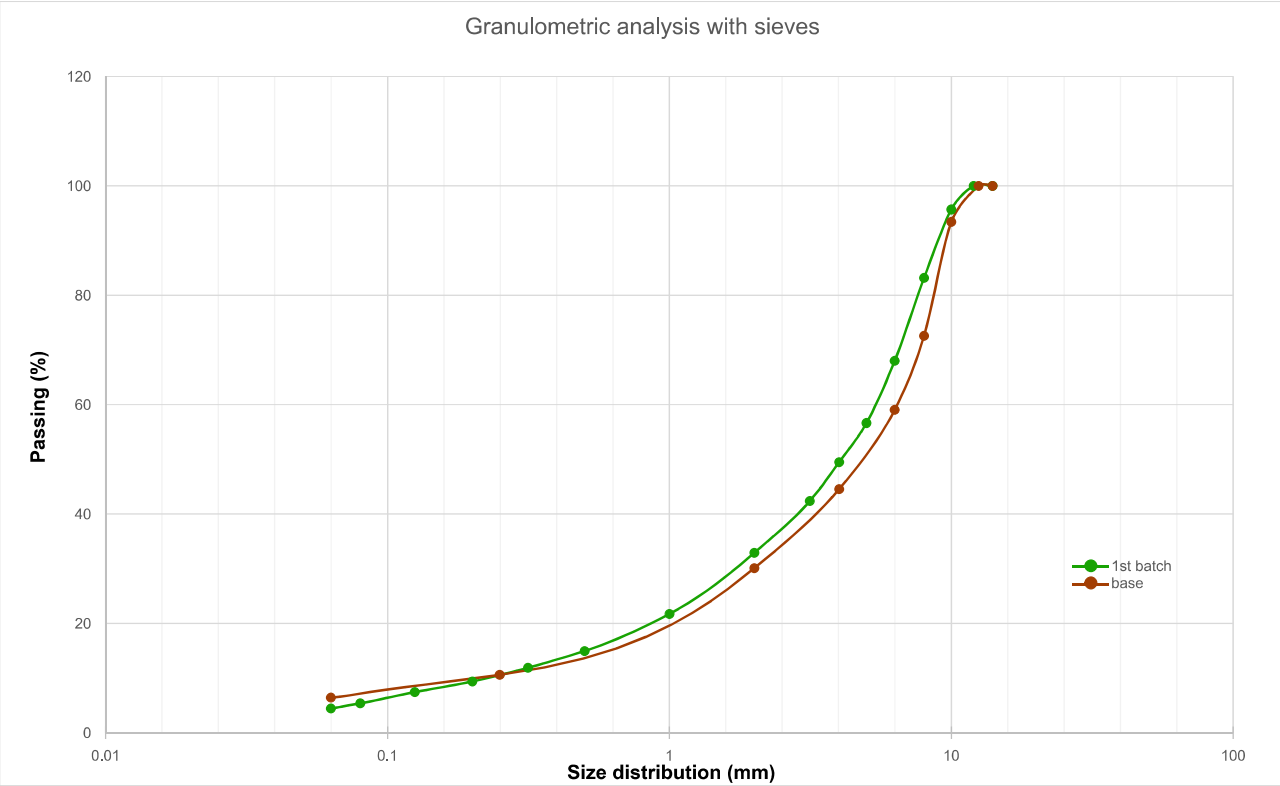

1st batch				
	Passing mass		Weighted mass on sieves	
Sieve [mm]	[g]	[%]	[g]	[%]
14	2836.9	100	0	0
12	2836.9	100	0	0
10	2714.3	95.67838	122.6	4.321618668
8	2359.3	83.16472	477.6	16.83527794
6.3	1929.2	68.00381	907.7	31.99619303
5	1606.7	56.63576	1230.2	43.36423561
4	1403.8	49.48359	1433.1	50.51640876
3.15	1202.1	42.37372	1634.8	57.62628221
2	933.7	32.91269	1903.2	67.08731362
1	616.6	21.73499	2220.3	78.26500758
0.5	424.2	14.95294	2412.7	85.04705841
0.315	337.2	11.88621	2499.7	88.11378618
0.2	266.4	9.390532	2570.5	90.60946808
0.125	211.1	7.441221	2625.8	92.55877895
0.08	152.7	5.382636	2684.2	94.61736402
0.063	125.9	4.437943	2711	95.56205718

Total mass [g] 2836.9

Formule	Sieve	20	16	14	12.5	10	8	6.3	4	2	0.25	0.063
	Int	#NOM?	#NOM?	#NOM?	#NOM?	#NOM?	#NOM?	#NOM?	#NOM?	#NOM?	#NOM?	#NOM?
	1st gran	100	100	100	100	95.837	81.938	65.9734	54.408	32.9056	9.54916	4.16299

Base granulometry	100	99.8	98.3	98	94	72	60	42	32	12	6.4
Variation	0	-0.2	-1.7	-2	-1.83701	-9.93803	-5.97342	-12.408	-0.90564	2.45084	2.23701

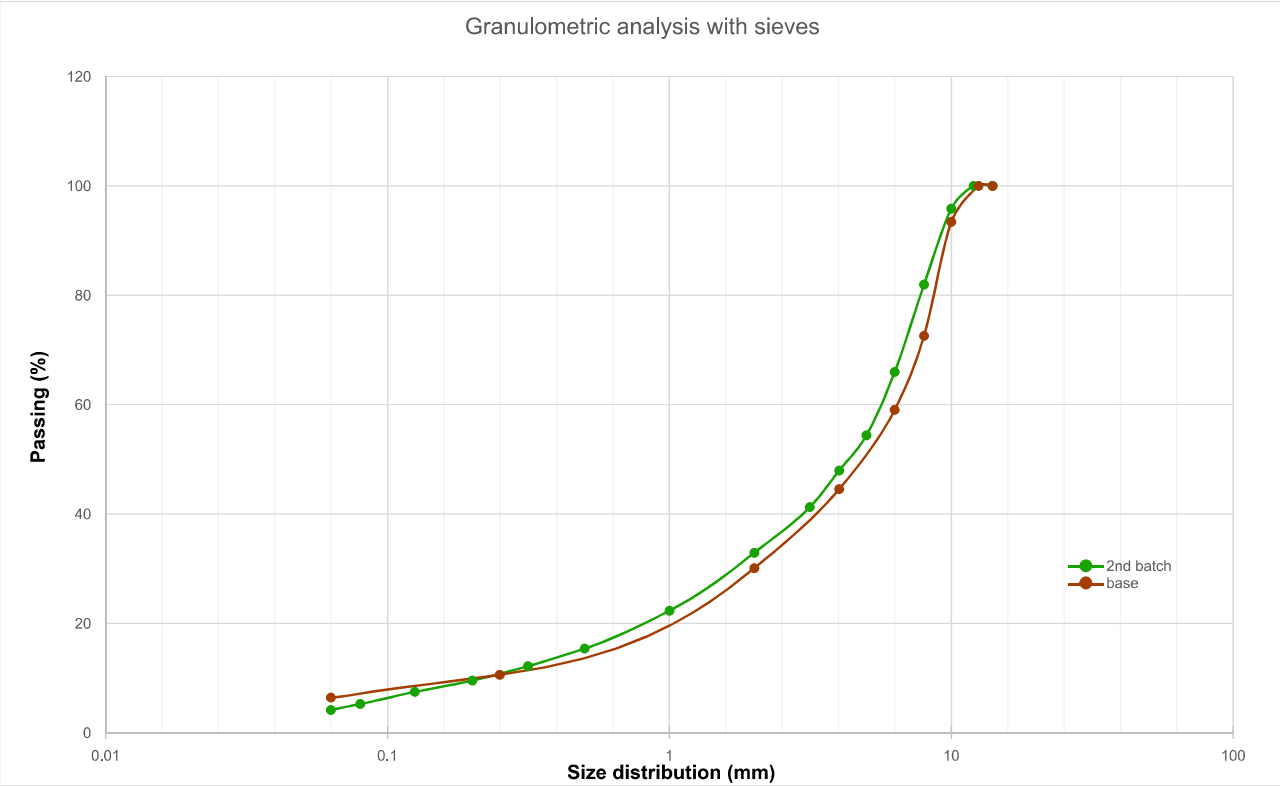

2nd batch				
	Passing mass		Weighted mass on sieves	
Sieve [mm]	[g]	[%]	[g]	[%]
14	2836.9	100	0	0
12	2836.9	100	0	0
10	2718.8	95.83701	118.1	4.162994818
8	2324.5	81.93803	512.4	18.06196905
6.3	1871.6	65.97342	965.3	34.02657831
5	1543.5	54.40798	1293.4	45.59201946
4	1359.8	47.9326	1477.1	52.06739751
3.15	1170.5	41.25983	1666.4	58.74017413
2	933.5	32.90564	1903.4	67.09436357
1	633.1	22.31661	2203.8	77.6833868
0.5	436.4	15.38299	2400.5	84.61701153
0.315	345.6	12.18231	2491.3	87.81768832
0.2	270.9	9.549156	2566	90.45084423
0.125	212.1	7.476471	2624.8	92.5235292
0.08	149.3	5.262787	2687.6	94.73721316
0.063	118.1	4.162995	2718.8	95.83700518

Total mass [g] 2836.9

Procédure d'exécution
Essais de terrassement et de chaussées en laboratoire

ANNEXE : Fabrication des enrobés

Réf : IF_(Pe-LEM-R1-MSC)3_34_FE_Fabrication des enrobés
Indice : vp1
Date application : 26/01/16
Page : 1/1

Département IRM **DIMA**

Formule étudiée :	**BBE (0/10)**	**Référence CEREMA :**
Appelation européenne :	**BBE 10 roulement-liaison**	

Fraction	Provenance	Dosage (%)	MVRg (Mg/m³)
0/2	Pont de colonne	26.1	2.65
2/6.3	Pont de colonne	23.7	2.63
6.3/10	Pont de colonne	42	2.63
Filler	calcaire	2.8	2.7
Chaux	Lhoist	0	2.24
Bitume résiduel	35/50	5.4	1.024
Emulsion C65	Probinord	8.31	1.01547
Eau d'ajout		2.6	1

Masse Volumique Calculée de l'enrobé (MVRe) : Mg/m³
Masse Volumique Réelle de l'enrobé (MVRe) : 2.2702 Mg/m³

Température de l'essai : ambiante °C

Données récup'
Questions

Masse Granulat + Bitume = 1805 g **Arrondi à :** 20000 g
X10 éprouvettes = 18053 g

Fraction	Dosage		Masse matériaux nécessaire :	
0/2	26.1	%	**5220**	**g**
2/6.3	23.7	%	**4740**	**g**
6.3/10	42	%	**8400**	**g**
Filler	2.8	%	**560**	**g**
Chaux	0	%	**0**	
Bitume résiduel	5.4	%	**1080**	**g**
Emulsion C65	8.31	%	**1662**	**g**
Eau d'ajout	2.6	%	**520**	**g**

Fabrication pour essais *PCG*
(Niveau 1)

Observation(s) : confection d'éprouvettes cylindriques d'environ 5 cm d'épaisseur et 15cm de diamètre à la PCG

Destinataire(s) :	**A Sourdun, Mai 2024** **Etabli par : Imanol BARREIRO**

Procédure d'exécution
Essais de terrassement et de chaussées en laboratoire

ANNEXE : Fabrication des enrobés

Réf : IF_(Pe-LEM-R1-MSC)3_34_FE_Fabrication des enrobés
Indice : vp1
Date application : 26/01/16
Page : 1/1

Département IRM **DIMA**

Formule étudiée :	**BBE (0/10)**	**Référence CEREMA :**
Appelation européenne :	**BBE 10 roulement-liaison**	

Fraction	Provenance	Dosage (%)	MVRg (Mg/m³)
0/2	Pont de colonne	26.1	2.65
2/6.3	Pont de colonne	23.7	2.63
6.3/10	Pont de colonne	42	2.63
Filler	calcaire	2.8	2.7
Chaux	Lhoist	0	2.24
Bitume résiduel	35/50	5.4	1.024
Emulsion C65	Probinord	8.31	1.01547
Eau d'ajout		2.6	1

Masse Volumique Calculée de l'enrobé (MVRe) : Mg/m³
Masse Volumique Réelle de l'enrobé (MVRe) : 2.2702 Mg/m³

Température de l'essai : ambiante °C

Données récup'
Questions

Masse Granulat + Bitume = 2166 **g** **Arrondi à :** **22500** **g**
X6 éprouvettes = **12998** **g**

Fraction	Dosage		Masse matériaux nécessaire :	
0/2	26.1	%	**5872.5**	**g**
2/6.3	23.7	%	**5332.5**	**g**
6.3/10	42	%	**9450**	**g**
Filler	2.8	%	**630**	**g**
Chaux	0	%	**0**	
Bitume résiduel	5.4	%	**1215**	g
Emulsion C65	8.31	%	**1869**	**g**
Eau d'ajout	2.6	%	**585**	**g**

Fabrication pour essais *PCG*
(Niveau 1)

Observation(s) : confection d'éprouvettes cylindriques d'environ 6 cm d'épaisseur et 15cm de diamètre à la PCG

Destinataire(s) :	**A Sourdun, Mai 2024** **Etabli par : Imanol BARREIRO**

	Procédure d'exécution Essais de terrassement et de chaussées en laboratoire **ANNEXE : Fabrication des enrobés**	**Réf :** IF_(Pe-LEM-R1-MSC)3_34_FE_Fabrication des enrobés **Indice :** vp1 **Date application :** 26/01/16 **Page :** 1/1

Département IRM **DIMA**

Formule étudiée :	**BBE (0/10)**	**Référence CEREMA :**
Appelation européenne :	**BBE 10 roulement-liaison**	

Fraction	Provenance	Dosage (%)	MVRg (Mg/m³)
6.3/10	Pont de colonne	42	2.63
2/6.3	Pont de colonne	23.7	2.63
0/2	Pont de colonne	26.1	2.65
Filler	calcaire	2.8	2.7
Chaux	Lhoist	0	2.24
bitume résiduel	Eurobitume	5.4	1.024
Emulsion C65	Probinord	8.31	1.01547
Eau d'ajout		2.6	1

Référence de la norme NF EN 13108-31 :

% de vide de la plaque : 12 88
Epaisseur de la plaque : 0.09 m

Masse Volumique Réelle de l'enrobé (MVRe) : 2.27 Mg/m³
Température de l'essai : ambiante

Masse Granulat + Emulsion = **20281.78** **g** **Arrondi à :** **21500** **g**

Fraction	Dosage (%)
6.3/10	42
2/6.3	23.7
0/2	26.1
Filler	2.8
Chaux	0
Emulsion C65	8.31
Eau d'ajout	2.6

Masse matériaux nécessaire :	
9030	**g**
5095.5	**g**
5611.5	**g**
602	**g**
0	**g**
1786.15	**g**
559	**g**

Fabrication pour essais d'orniérage
(Niveau 2)

Observation(s) : confection d'éprouvette de type plaque

Destinataire(s) :	**A Sourdun. Juillet 2024** **Etabli par :** *Imanol BARREIRO*

Eprouvette	B1 (en mm)	B2 (en mm)	H1 (en mm)	H2 (en mm)	Hauteur (en mm)
1	40.83	40.91	40.8	40.95	120.25
2	39.95	40.32	40.09	40.67	120.36
3	40.66	40.45	40.7	40.1	120.47
4	40.13	39.8	40.67	39.81	119.81
5	40.86	40.8	41.09	41.31	120.59
6	41.34	40.81	40.7	40.84	120.94

Eprouvette	Pesée air (g)	Pesée eau (g)	Volume ($g.m^3/Mg$)	Mva (Mg/m^3)	Compacité (en %)	% de vide	Mva moyenne
1	425.5	229.3	196.59	2.16	95.34	4.66	2.16
2	412.1	220.7	191.78	2.15	94.65	5.35	
3	419.6	226.5	193.49	2.17	95.53	4.47	
4	405.6	217.9	188.08	2.16	94.99	5.01	
5	433.1	234.8	198.70	2.18	96.01	3.99	
6	428.9	231.3	198.00	2.17	95.42	4.58	

	1st fabrication	2nd fabrication
Series	1	2
Protocoles	Temperature 20°C and 5mm/min	Temperature 5°C and 5mm/min
Specimens	10_a	6_a
	2_a	6_b
	2_b	7_a
	3_a	7_b
	3_b	8_a
	4_a	8_b
	4_b	9_a
	5_a	9_b
	10_b	5_b
	11_a	13_b
	11_b	14_a
	12_a	14_b
	12_b	15_a
	13_a	15_b

Series	1	2
Protocoles	Temperature 20°C and 5mm/min	Temperature 5°C and 5mm/min
Specimens	5.839421256	5.661327092
	5.801069056	6.189681978
	5.451430993	5.49446645
	4.373202016	5.478372888
	4.853202176	4.883479167
	5.318247798	5.002621963
	5.727524896	5.084453913
	4.825212159	5.161858222
	5.581650799	4.232550322
	6.245440676	6.215535425
	6.116058189	6.593858044
	6.987716117	6.651290869
	6.029882037	6.294075508
	5.655129781	6.476373089
Average	5.63	5.67
Standard deviation	0.5	0.4

G- Maxwell parameters	
E_i	τ_i
231.63308	∞
646.182021	7.20E-10
531.877507	4.15E-09
606.270581	1.74E-08
735.129014	7.63E-08
864.100135	3.41E-07
1018.37601	1.60E-06
1103.4341	7.86E-06
1211.54684	3.74E-05
1297.69473	0.00018132
1290.65982	0.00081466
1267.83935	0.0033111
1210.43898	0.01256603
1003.94769	0.0484456
636.349147	0.18612949
336.950769	0.69551344
175.496273	2.65166431
99.1753841	12.6915206